

On the Order Reduction of the Radiative Heat Transfer Model for the Simulation of Plasma Arcs in Switchgear Devices

Lorenzo Fagiano and Rudolf Gati

***Abstract*—An approach to derive low-complexity models describing thermal radiation, employed to simulate the behavior of electric arcs in switchgear systems, is presented. The idea is to approximate the (high dimensional) full-order equations, describing the propagation of the radiated heat intensity in space, with a model of much lower dimension, whose parameters are identified by means of nonlinear system identification techniques. The proposed order reduction approach is able to systematically compute the partitioning of the electromagnetic spectrum in frequency bands, and the related absorption coefficients, that yield the best matching with respect to the finely resolved absorption spectrum of the considered gaseous medium. In addition to the order reduction approach and the related computational aspects, an analysis by means of Laplace transform is presented, providing a justification to the use of very low orders in the reduction procedure as compared with the full-order model. Finally, comparisons between the full-order model and the reduced-order ones are presented.**

***Index Terms*—Arc simulations, Radiative heat transfer, Model order reduction, Nonlinear estimation, Nonlinear model identification**

I. Introduction

The switching performance of circuit breakers depends strongly on the behavior of the electric arc that originates when the contacts are opened in presence of relatively large electric current values [36], [8]. In turn, the arc dynamics are influenced by multiple interacting physical phenomena which, together with the short timescale of the arcing event and the large values of temperature and pressure, increase the complexity and difficulty of understanding, carrying out experiments, and deriving numerical models of the switching behavior. Computational fluid dynamic (CFD) approaches are being used in both public and private research efforts to simulate the time evolution of the plasma that carries the current during the interruption process, see e.g. [13], [6], [2], [18]. The CFD simulations are often coupled with solvers for the electro-magnetic (EM) phenomena, resulting in sophisticated multi-physics simulation tools (see [6], [18]) that allow one to gather an insight of what is actually happening during the current interruption process - aspects that are very difficult to quantify with direct measurements, for the above-mentioned reasons. Such simulation tools provide a significant added value to explain the results of experimental tests and to support the development of switchgear devices, however they also bring forth an important issue in addition to the inherent difficulty of plasma modeling: the need to find a good balance between the accuracy of the employed physical models and their computational complexity. The modeling of radiative heat transfer during the arcing process is an illuminating example of such an issue.

The authors are with ABB Switzerland Ltd., Corporate Research, 5405 Baden-Dättwil - Switzerland

E-mail addresses: {lorenzo.fagiano | rudolf.gati}@ch.abb.com

Radiation is one of the most important cooling mechanisms during switching, as it redistributes the heat produced by the current flowing through the plasma and transfers part of this power to the boundaries. Hence, accurate models of radiation are of fundamental importance to simulate the arc behavior, which is, due to the physics of radiation at the temperatures present in the plasma, a challenging task. Typically, the core of the arc is heated up to 25,000 K, meaning that the EM radiation emitted by ions, atoms, and molecules of several different species (e.g. nitrogen, oxygen, or copper) have to be taken into account. The relevant window of the EM spectrum ranges from $3\,10^{13}$ Hz-$6\,10^{15}$ Hz, corresponding to wavelengths between 10^{-5} m and $5\,10^{-8}$ m, i.e. from infrared to ultraviolet. The main difficulty in simulating the EM radiation emitted by an arc derives from the complexity of the emission spectrum, where the relevant property, the absorption coefficient, changes by many orders of magnitude at spectral lines of which several 10,000 exist in the range under consideration. The propagation of radiative heat in space for each frequency is modeled, under assumptions that are reasonable for the arcing phenomena encountered in switchgear devices, by a first-order differential equation taking into account the absorption and the emission of radiation along the direction of propagation. The energy removed from the arc is with this defined by the temperature, pressure, and composition distribution within. Due to the complexity of the emission spectrum, a simple discretization according to frequencies leads to hundred thousands of very thin frequency bands; within each one of such bands the absorption coefficient can be assumed to be constant for fixed temperature, pressure and composition of the gaseous medium. This, however, leads to the same number of three dimensional field equations which need to be solved. Given the large number of finite volumes that have to be considered in CFD simulations of realistic geometries (see e.g. [28]), the use of such a large-scale radiation model is not feasible. Hence, there is the need to derive models for the radiative heat transfer with much lower complexity, possibly without compromising too much the accuracy as compared with the large-scale model.

This issue has been tackled by several contributions in the literature [19], [30], [15], [26]. Most of the existing approaches consist in discretizing the fraction of the EM spectrum of interest into few bands, and assuming for each one some averaged absorption properties. The mentioned approaches have the advantage of being quite simple to implement, however in principle one should optimally choose ad-hoc different bands and averaged absorption coefficients as a

function of pressure, temperature and chemical composition of the considered medium, since the radiation parameters are affected by all these aspects. If the bands and/or the averaged absorption coefficients are not chosen in an appropriate way, the model accuracy is worse and more bands are needed to improve it, resulting in a relatively large number of bands (6-10) in order to achieve accurate results with respect to the original, large-scale model. Hence, this procedure can be time consuming, not trivial to carry out in a systematic way, and ultimately suboptimal in terms of complexity/accuracy compromise.

In this paper, we present a new approach to derive small-scale, band-averaged models of the radiative heat transfer. We first describe the problem of radiation modeling from a novel perspective, where the aim is to approximate the input-output behavior of a large scale, linear-parameter-varying (LPV) dynamical system with that of a low-order one. The large scale system has one input (black-body intensity), one output (radiated intensity), three scheduling parameters (temperature, pressure and composition), and a large number of internal states (one for each considered frequency of the EM spectrum), while the low-order LPV system has the same input, output and scheduling parameters, but just a handful of internal states. From this point of view, the problem can be classified as a model-order reduction one [23]. Then, using classical tools for the analysis of signals and dynamical systems, we provide evidence that indeed models with quite low order (typically 2-3 bands) can be already good enough to capture the main behavior of the full-order model. Finally, we tackle the order reduction problem by using nonlinear system identification techniques (see e.g. [24]), where we collect input-output data from the large-scale system and use it to identify the parameters of the reduced-order model. The approach results in a nonlinear optimization problem (nonlinear program - NLP) with a smooth non-convex cost function and convex constraints, which are needed to preserve the physical consistency of the reduced-order model. We show through examples that the obtained reduced-order models enjoy a high accuracy with respect to the full-order one, while greatly reducing the computational times. As compared with the existing approaches, the method proposed here has the significant advantage of being systematic, i.e. there is no need to tailor or tune it for each different composition of the absorbing/emitting medium. The main user-defined parameter is the desired number of frequency bands in the reduced-order model, which can be then increased gradually until the desired tradeoff in terms of model quality vs. complexity is reached.

The paper is organized as follows. Section I-A collocates the present work in the wider context of arc simulation activities carried out at ABB Corporate Research to support the development of switchgear. Section I-B provides a formal description of the problem we tackle. In Section II, such a problem is analyzed from a system's perspective and connections are made to the order reduction of a large-scale LPV dynamical system. The proposed computational approach is described in Section III, finally results are presented in Section IV and conclusions and future developments are discussed in Section V.

A. The Arc Simulation Tool

The Arc Simulation Tool is a simulation suite developed at ABB Corporate Research with the aim to model the behavior of electric arcs in switchgear, [28], [9]. In the tool, the electric arc is treated using the magneto hydrodynamic (MHD) approach [34], [31], where the dynamics of electrically conductive fluids are represented combining the Reynolds-averaged Navier-Stokes (for the fluid part) and Maxwell (for the EM part) equations. In addition, equations for the radiative heat transfer are computed, since one of the dominant energy redistribution processes inside the arc is due to EM radiation [35]. Plasma properties such as enthalpy, density or electrical conductivity as functions of the local temperature, pressure, and composition are accounted for by means of pre-computed real gas tables [16], [14]. Local thermodynamic equilibrium (LTE) is assumed to hold everywhere in the plasma and a possible presence of space charges is neglected. The system of equations is closed with a set of appropriate boundary conditions, where particular care is taken in the modelling of ablating polymeric walls and eroding metallic surfaces [7], [17]. The motion of contacts inside the computational domain and the external network providing a current to the device are taken into account in our model with suitable differential equations. The equations are simplified to enable faster computations. In particular, the solution of the fluid dynamic field distributions is only weakly coupled to the EM computations. The transient flow equations are solved in a first step using the commercial finite volume solver Ansys Fluent®, where the EM contributions such as the Ohmic heating or Lorentz force are accounted for as external sources. The resulting electrical conductivity distribution is exported to an ABB in-house developed EM finite elements solver, [29]. The solution of the electrostatic and magnetostatic problems (taking into account the magnetic saturation of ferromagnetic materials, resulting in a nonlinear B-H curve) is then fed back to the flow simulation. Three different species are modelled in the plasma: air, metal, and polymers. Presently, copper and silver are implemented and experimentally validated. A condensation model for the metallic plasma is also present. The ablation of polymeric walls is described by a simple, phenomenological model. Here, hydrogen atoms (or alternatively methylene groups, CH2) are detached from the polymeric chains due to the heat input from the arc and are responsible for the pressure build up in front of the isolating walls. Thermal radiation is treated by using the photo-hydrodynamic model, see e.g. [12]. To provide an example of the accuracy with which the tool is able to reproduce experimental findings, Fig. 1 shows a comparison between the simulated arc voltage and the measured one, during a short-circuit test with an ABB circuit breaker. The main advantage of the simulation tool is to provide insight to what is actually happening inside the device during interruption. Such a knowledge is then exploited to improve the design and generate new ideas. A crucial aspect of radiation modeling is the reduction of the large-scale system of equations, which describe the heat transported by each frequency of the EM spectrum, into a small-scale one, in order to make it possible to resolve the resulting photo-hydrodynamic system in CFD simulations. In the arc simulation tool, this problem is addressed by a novel, optimization-based approach, presented in detail in this paper.

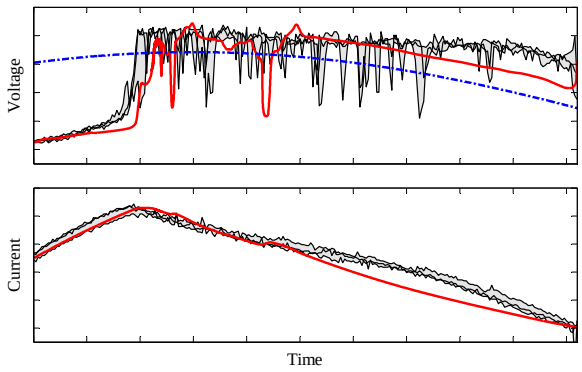

Fig. 1. Comparison between simulated results (red solid line) and the envelope of several experimental tests (gray band) for an ABB air circuit breaker. Dash-dot line: voltage of the generator driving the circuit. The scales of time, current and voltage are not shown for confidentiality reasons.

B. Problem formulation

Let us consider a region in space containing a hot gaseous mixture of $r \in \mathbb{N}$ different components. Each component is present in a fraction (e.g. of mass or of mole) $y_i \in [0,\, 1]$, $i = 1, \ldots, r$,. We indicate with $y = [y_1, \ldots, y_r]^\top$ the composition vector of the medium, where $^\top$ stands for the matrix transpose operation. We consider a line of propagation along which we want to compute the radiated heat, and denote with $x \in \mathbb{R}$ the position of a point lying on such a line. As the line crosses the hot matter, the temperature $T(x) \in \mathbb{R}^+$, pressure $p(x) \in \mathbb{R}^+$ and composition $y(x) \in [0,\, 1]^r$ change with x (see Figure 2 for a graphical visualization). The temperature, pressure and

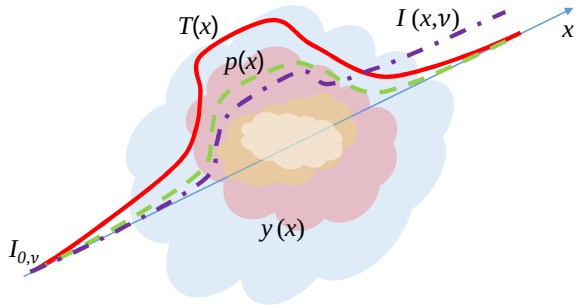

Fig. 2. Sketch of the considered problem. The aim is to compute the spatial distribution of the radiated intensity $I(x, \nu)$ (dash-dotted line) for a given frequency ν of the EM spectrum through a gaseous medium along a given direction with coordinate x. The temperature T (solid line), pressure p (dashed) and composition y (balloons of different colors) of the gas depend on x. The intensity at $x = 0$, $I_{0,\nu}$, is a known initial condition.

composition of the gas lie in some sets of interest, $\mathcal{T}$, $\mathcal{P}$ and $\mathcal{Y}$ respectively, defined as follows:

$$\begin{aligned} \mathcal{T} &= [T_{\min},\, T_{\max}] \subset \mathbb{R}^+ \\ \mathcal{P} &= [p_{\min},\, p_{\max}] \subset \mathbb{R}^+ \\ \mathcal{Y} &= \left\{ y \in [0,\, 1]^r : \sum_{i=1}^{r} y_i = 1 \right\} \end{aligned} \tag{1}$$

Typical values defining the sets $\mathcal{T}$ and $\mathcal{P}$ are $T_{\min} = 300\,\mathrm{K}$, $T_{\max} = 25,000\,\mathrm{K}$, $p_{\min} = 10^4\,\mathrm{Pa}$ and $p_{\max} = 10^7\,\mathrm{Pa}$.

Considering local thermodynamic equilibrium and assuming, without loss of generality, that at $x = 0$ the radiated heat intensity, for a given frequency ν of the EM spectrum, is equal to a given value $I_{\nu,0}$, the distribution of the intensity as a function of x can be computed through the following ordinary differential equation:

$$\begin{aligned} &\frac{dI(x,\nu)}{dx} = \alpha\left(T(x), p(x), y(x), \nu\right)\left(I_{bb}(T(x),\nu) - I(x,\nu)\right), \\ &I(0,\nu) = I_{\nu,0}, \end{aligned} \tag{2}$$

where $\alpha(\cdot,\cdot,\cdot,\nu)$ is the absorption coefficient and $I_{bb}(\cdot,\nu)$ is the black body intensity, both pertaining to the frequency ν. For a fixed value of ν, α depends on temperature, pressure and composition, while I_{bb} is a function of temperature only.

In equation (2), it is implicitly assumed that the radiation distribution has already converged to a steady state. Since the temporal dynamics of the radiated heat are much faster than the timescale of the phenomena of interest in arc simulations, such an assumption is reasonable. Similarly, scattering effects have been also neglected as they represent a negligible term for the application considered here. For a more complete form of equation (2) the interested reader is referred to [35].

Thus, for each frequency ν the corresponding ODE (2) is characterized by two parameters, namely the black body intensity I_{bb} and the absorption coefficient α. The dependency of the latter on $T(x)$, $p(x)$, $y(s)$ renders the equation nonlinear. From a physical perspective, the black body intensity is a source of radiation, while the current intensity $I(x,\nu)$ is a sink: the change of radiated intensity in an infinitesimal space interval dx is the difference between these two contributions, scaled by the absorption coefficient. The black-body intensity as a function of the frequency ν and of temperature T is given by Planck's law [35]:

$$I_{bb}(T,\nu) = \frac{2\,h\,\nu^3}{c^2} \frac{1}{e^{\frac{h\,\nu}{k_B\,T}} - 1}, \tag{3}$$

where $h \simeq 6.62\,10^{-34}\,\mathrm{J\,s}$ is the Planck constant, $c \simeq 10^8\,\mathrm{m\,s^{-1}}$ is the speed of light in vacuum and $k_B \simeq 1.38\,10^{-23}\,\mathrm{J\,K^{-1}}$ is the Boltzmann constant. The behavior of $I_{bb}(T,\nu)$ as a function of ν for some temperature values is shown in Figure 3. For the purpose of this study, the total black-body intensity $\overline{I}_{bb}(T)$ per unit of surface and solid angle (black-body radiance) is also needed, given by Stefan-Boltzmann's law:

$$\overline{I}_{bb}(T) \doteq \int_0^\infty I_{bb}(T,\nu)d\nu = \frac{\sigma_{SB}}{\pi} T^4 \tag{4}$$

where $\sigma_{SB} \simeq 5.67\,10^{-8}\,\mathrm{W\,m^{-2}\,K^{-4}}$ is the Stefan-Boltzmann constant. From equation (3) and Figure 3 it can be noted that, for the temperature values of interest for arc simulations in circuit breakers (3,000K-25,000K), most of the black-body radiance (i.e. the area below the solid curves in Figure 3) is contributed by the frequencies in the range of approximately $3\,10^{13}$ Hz-$6\,10^{15}$ Hz.

While the dependence of the black-body intensity on ν and T is well-known from the above physical laws, the absorption coefficient α is a much more uncertain quantity. Gaseous

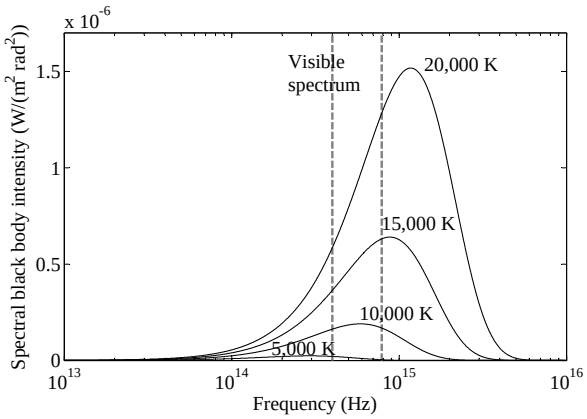

Fig. 3. Planck's law (3) (solid lines) computed for different temperature values. The frequency band of visible light is also shown (between gray dashed lines).

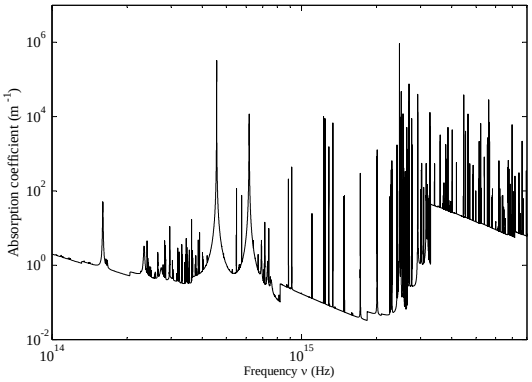

Fig. 4. Example of absorption spectrum for a mixture of 50% silver, 25% air and 25% hydrogen at 16,300 K and 10^5 Pa.

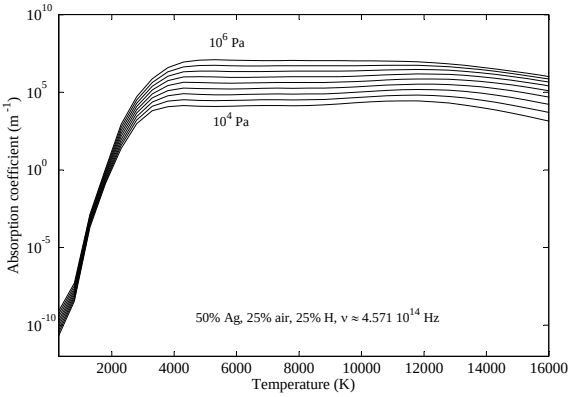

Fig. 5. Example of absorption coefficient for a mixture of 50% silver, 25% air and 25% hydrogen as a function of temperature and pressure, for $\nu = 4.571\,10^{14}$ Hz.

media have absorption spectra (i.e. the function relating α to ν) characterized by sharp lines at specific frequencies, whose values depend on the composition of the mixture and whose number is typically very large. Moreover, the absorption coefficient at each of such frequencies depends strongly on temperature and (less markedly) on pressure. Broadening effects due to pressure are also important as they contribute to a spread of the absorption lines over the nearby frequencies. Physical models to capture such complex absorption spectra have been proposed in the literature, [4], [21], [3], [10]. Moreover, databases of experimentally measured absorption data for several mixtures in specific frequency bands are available, typically for relatively low temperatures [27]. In the following, we will assume that α is a known function of T, p, y, ν, in the domain of interest; we call such information the "base data" $\mathcal{D}$:

$$\mathcal{D} \doteq \left\{\alpha(T,p,y,\nu);\ \forall T \in \mathcal{T},\ \forall p \in \mathcal{P},\ \forall y \in \mathcal{Y},\ \forall \nu \in \mathbb{R}^+\right\} \tag{5}$$

As an example of information contained in $\mathcal{D}$, Figure 4 shows the absorption spectrum for a mixture of 50% silver, 25% air and 25% hydrogen at 16,300 K and 10^5 Pa. For a fixed frequency of such a spectrum, Figure 5 shows the corresponding absorption coefficient as a function of temperature and pressure (note the logarithmic scale for the absorption coefficient in this plot).

Given the base data, the total radiated heat intensity $I_{tot}(x)$ is computed by integrating the intensity contributed by each frequency of the EM spectrum:

$$I_{tot}(x) \doteq \int_0^\infty I(x,\nu)d\nu. \tag{6}$$

In order to obtain a tractable problem, a first step is to adopt a fine discretization of the frequency domain such that (6) becomes a sum over a finite number of terms. Since the radiated intensity is relevant only in a specific region of the spectrum (compare Figure 3), the frequency discretization can be coarser outside such a region and finer inside, in particular around the peaks of the absorption spectrum. In this way, a finite number N of frequency values ν_i, $i = 1,\ldots,N$ are considered, each one being the middle point of an interval $\Delta\nu_i$ of the spectrum. Then, equation (6) can be re-written as:

$$I(x) \simeq \sum_{i=0}^{N} I(x,\nu_i)\Delta\nu_i. \tag{7}$$

Equation (7), together with (2)-(3) and with the base data $\mathcal{D}$ (5) evaluated at $\nu_i, i = 1,\ldots,N$, form a high-dimensional model of the radiated heat intensity, named the Full-Order Model (FOM). The high dimensionality of the FOM comes from the fact that a large number N of frequencies is taken into account in the discretization, so that the approximation error is small. Typical values of N for the conditions of our interest are in the order of 1-2 10^5. Due to the large number of considered frequencies, the FOM can be used effectively only in very simple cases, for example in one-dimensional problems. In fact, in order to solve the radiative distribution in two- and three-dimensional cases, as it is needed for example in CFD simulations of real devices, one would have to solve many equations (whose nature depends on the chosen method, like the so-called P-N methods, the discrete ordinate method or the photohydrodynamic approach, see [35], [12]) for each one of the considered frequencies, leading quickly to an intractable

problem. In this paper, we tackle this issue by deriving a method to compute low complexity models for the radiative heat transfer. More specifically, we consider the following problem:

Problem 1: : Given the full-order model defined by (2)-(3), (7) and the base data $\mathcal{D}$, derive a model with the same structure, i.e. where the total intensity is the sum of a finite number of contributions obtained by partitioning the frequency domain, but where the number of such partitions is very small, while still capturing accurately the total radiated heat intensity. We call such a simplified model the Reduced-Order Model (ROM). The ROM can then be effectively used to model the propagation of heat via radiation in many applications, including full three-dimensional simulations of plasma arcs encountered in switchgear devices.

We remark that, in light of Problem 1, in this work we will consider the radiated intensity computed with the FOM as "exact". We will thus evaluate the quality of a given ROM by assessing the discrepancy between the radiative heat intensity given by the latter and the one given by the FOM. In other words, we don't consider here the accuracy of the FOM with respect to the real-world behavior of gaseous media. Indeed, the topic of modeling accurately and/or measuring the absorption spectrum of a given gas as a function of temperature and pressure (i.e. to compute the base data $\mathcal{D}$) is by itself an important and active research area [4], [21], [3], [10], however it is outside the scope of this work, which is focused on the simplification of the FOM into a computationally tractable model. On the other hand, the method presented in this paper does not depend on the specific absorption spectrum, i.e. it can be applied systematically to any base data, and it yields quite small discrepancies between the derived ROM and the employed FOM, such that the error between the ROM and the real behavior of the considered medium depends ultimately only on the quality of the FOM.

II. A SYSTEM'S PERSPECTIVE OF RADIATIVE HEAT TRANSFER

A. Equivalent input-output models of the radiative heat transfer

As a preliminary step to address Problem 1, we re-write the FOM in a slightly different form, which is convenient to show that this model can be seen as a single-input, single-output (SISO) Linear Parameter-Varying dynamical system. Let us define the spectral emissivity $e(T,\nu)$ as:

$$e(T,\nu) \doteq \frac{I_{bb}(T,\nu)}{\overline{I}_{bb}(T)}, \tag{8}$$

i.e. the ratio between the total black body intensity and the one pertaining to each frequency of the EM spectrum. By construction we have $e(T,\nu) \in (0,1),\ \forall (T,\nu) \in \mathcal{D}$ and $\int_\nu e(T,\nu)d\nu = 1\,\forall T$. The course of $e(T,\nu)$ is illustrated in Figure 6.

By inserting the spectral emissivity (8) in equation (2), the radiated heat intensity for each frequency value $\nu_i, i = 1,\dots,N$ of the FOM can be equivalently computed as:

$$\begin{aligned}&\frac{dI(x,\nu_i)}{dx} = \\ &\alpha\left(T(x),p(x),y(x),\nu_i\right)\left(e(T(x),\nu_i)\overline{I}_{bb}(T(x)) - I(x,\nu_i)\right),\\ &I(0,\nu_i) = I_{\nu_i,0}.\end{aligned} \tag{9}$$

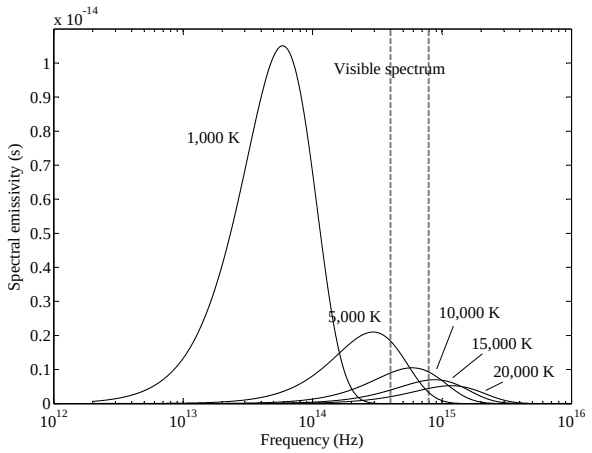

Fig. 6. Spectral emissivity $e(T,\nu)$ as a function of EM frequency (solid lines), computed for different temperature values. The frequency band of visible light is also shown (between gray dashed lines).

Equation (9) is just a re-writing of (2) but, together with equation (7), it highlights the fact that the FOM can be seen as a dynamical system where x is the independent variable, $T(x)$ is an exogenous scalar input, $I(x,\nu_i), i = 1,\dots,N$ are N internal states, $I_{tot}(x)$ a scalar output, and $p(x), y(x)$ are space-dependent parameters. In virtue of the fact that the function relating the temperature T to the total black-body intensity $\overline{I}_{bb}$ is known, one can consider the latter as input to the system hence putting into evidence the Linear Parameter Varying (LPV) structure of the model:

$$\begin{aligned}\frac{d\overline{I}(x)}{dx} &= A(T(x),p(x),y(x))\,\overline{I}(x)\\ &\quad + B(T(x),p(x),y(x))\,\overline{I}_{bb}(T(x))\\ I_{tot} &= C\,\overline{I}(x),\end{aligned} \tag{10}$$

where

$$\begin{aligned}\overline{I}(x) &\doteq [I(x,\nu_1),\dots,I(x,\nu_N)]^\top \in \mathbb{R}^{N\times 1}\\ A(T,p,y) &\doteq \text{diag}([-\alpha(T,p,y,\nu_1),\\ &\quad \dots,-\alpha(T,p,y,\nu_N)]^\top) \in \mathbb{R}^{N\times N}\\ B(T,p,y) &\doteq [\alpha(T,p,y,\nu_1)e(T,\nu_1),\\ &\quad \dots,\alpha(T,p,y,\nu_N)e(T,\nu_N)]^\top \in \mathbb{R}^{N\times 1}\\ C &\doteq [\Delta\nu_1,\dots,\Delta\nu_N] \in \mathbb{R}^{1\times N}.\end{aligned} \tag{11}$$

A block-diagram of the FOM from this new point of view is shown in Figure 7(a). Such a system's perspective of the radiative heat transfer equations is the fundamental step at the basis of all the developments described in the remainder of this paper. We can now introduce more precisely the structure of a candidate reduced-order model (ROM) meant to approximate the FOM. Let us denote the *bands* of the ROM with $\mu_1,\dots,\mu_M$, with $M \ll N$ (e.g. $M = 2$), and the corresponding vector of inner states with $\hat{\overline{I}}(x) \doteq [\hat{I}(x,\mu_1),\dots,\hat{I}(x,\mu_M)]^\top \in \mathbb{R}^{M\times 1}$. Then, we can write the equations describing the ROM as:

$$\begin{aligned}\frac{d\hat{\overline{I}}(x)}{dx} &= \hat{A}(T(x),p(x),y(x))\,\hat{\overline{I}}(x)\\ &\quad + \hat{B}(T(x),p(x),y(x))\,\overline{I}_{bb}(T(x))\\ \hat{I}_{tot}(x) &= \hat{C}\,\hat{\overline{I}}(x),\end{aligned} \tag{12}$$

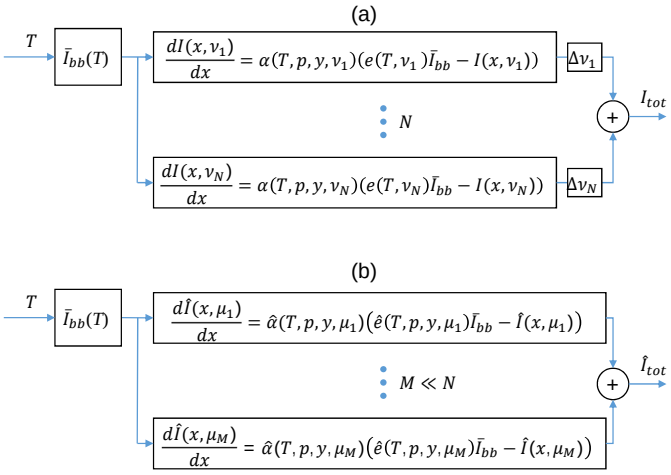

Fig. 7. Equivalent block diagram of the (a) full-order model, FOM, and (b) reduced-order model, ROM. The dependence of T, p, y on x is omitted for the sake of readability.

where

$$\begin{aligned}\hat{A}(T,p,y) &\doteq \text{diag}([-\hat{\alpha}(T,p,y,\mu_1),\\ &\quad \ldots,-\hat{\alpha}(T,p,y,\mu_M)]^\top) \in \mathbb{R}^{M\times M}\\ \hat{B}(T,p,y) &\doteq [\hat{\alpha}(T,p,y,\mu_1)\hat{e}(T,p,y,\mu_1),\\ &\quad \ldots,\hat{\alpha}(T,p,y,\mu_M)\hat{e}(T,p,y,\mu_M)]^\top \in \mathbb{R}^{M\times 1}\\ \hat{C} &\doteq [1,\ldots,1] \in \mathbb{R}^{1\times M}.\end{aligned} \tag{13}$$

Figure 7(b) gives a graphical representation of the ROM. Practically speaking, from (12)-(13) one can see that each component of vector $\hat{\bar{I}}(x)$ accounts for a certain portion of the total radiated heat intensity, in complete analogy with the FOM (10), the only difference being the number of frequency bands, which in the ROM is much smaller than in the FOM. For each band μ_i, the parameters $\hat{\alpha}(T,p,y,\mu_i)$ and $\hat{e}(T,p,y,\mu_i)$ have thus the meaning of "equivalent" absorption coefficient and spectral emissivity, respectively. Here, we use the term "equivalent" since these parameters have the same role, in the differential equations describing the ROM, that the original parameters $\alpha(T,p,y,\nu_i)$, $e(T,p,y,\nu_i)$ have in the equations pertaining to the FOM.

The task of deriving a ROM for the radiated heat transfer from the FOM is referred to as *model order reduction*. Computing a ROM is equivalent to assigning suitable values to $\hat{\alpha}$ and $\hat{e}$ as a function of the underlying parameters T, p, and y. In particular the collection of all bands has to form a non-overlapping partition covering the whole EM spectrum. Then, the value of $\hat{e}(T,p,y,\mu_i)$ has to correspond to the integral of the spectral black body intensity (3) over the frequency band pertaining to μ_i. Hence, one can equivalently state that computing a ROM amounts to choose, for each pair of pressure and composition values, a partition of the EM spectrum (which defines the equivalent emissivity as a function of temperature) and the courses of the corresponding equivalent absorption coefficients as a function of temperature. In previous contributions in the literature, e.g. [26], [30], the task of defining the ROM has been carried out by picking a finite number of bands covering the EM spectrum and then computing the equivalent absorption coefficients $\hat{\alpha}(T,p,y,\mu_i)$ through some averaging procedure on the portion of the absorption spectrum contained in each band. This approach is simple to implement but it has the drawback of not being systematic, since both the choice of the band cuts and the averaging of the absorption coefficients have to be made by the user, without an immediate link to the accuracy of the resulting ROM. In the next sections, we will present a new order reduction approach to compute the partitioning of the EM spectrum and the values of $\hat{\alpha}(T,p,y,\mu)$ in a systematic way, that yields quite accurate results as compared with the FOM.

About this last point, i.e. the accuracy of the ROM, we note that the input of the FOM and of the ROM is exactly the same, corresponding to the total black-body radiation for the considered temperature profile, $\bar{I}_{bb}(T(x))$. Therefore, it is quite intuitive that the discrepancy between the total intensity given by the FOM, $I_{tot}(x)$, and the one predicted by the ROM, $\hat{I}_{tot}(x)$, for the same temperature profile $T(x)$ (i.e. the same distribution of $\bar{I}_{bb}(T(x))$), represents a reasonable indicator of the accuracy of the reduced-order model. In other words, the error signal $\Delta I(x) \doteq I_{tot}(x) - \hat{I}_{tot}(x)$ will be considered to evaluate the goodness of a given ROM. This choice is motivated by the fact that the total radiated heat intensity is the main quantity of interest predicted by the ROM when it is embedded in multi-physics simulations of arc plasma, since it is used to compute the heat transferred from the plasma volume to the walls, and also (through its divergence) the heat redistributed within the plasma volume. Hence, the ROM should reproduce this quantity as accurately as possible with respect to the FOM, given the same spatial distribution of temperature, pressure and chemical composition.

Before going to the details of the proposed method to derive the ROM, a sensible question to be addressed is whether the approximation problem we are dealing with has a reasonably good solution or not. More specifically, recall that we aim to approximate the input-output behavior of a large scale system, with hundred of thousands of internal states, with that of a small-scale one, with at most a handful of internal states. It is not immediately clear if there exist such a low-order ROM still capable of delivering high approximation accuracy, since this aspect depends on the characteristics of the FOM, i.e. on the underlying physics of the radiative heat transfer. In the next section, we exploit the system's perspective described above to provide an intuition that indeed a ROM with a handful of bands can capture most of the input-output behavior of the FOM.

B. Frequency-domain analysis

Analyzing the complexity of the FOM in its form (10) in the domain of position x is not straightforward due to the very large number of internal states, each one following its own dynamic evolution. Besides noticing that the FOM is given by the sum of a large number of non-interacting, asymptotically stable first-order systems, all driven by the same input and whose (position dependent) poles are given by $-\alpha(T,p,y)$, little more can be said.

However, if we consider fixed values of temperature, pressure and composition, $\overline{T}, \overline{p}$ and $\overline{y}$ respectively, and we assume that only infinitesimal perturbations of temperature take place

in space, such that the absorption properties of the medium can be assumed constant, we immediately notice that the FOM becomes a linear-parameter-invariant (LPI) system, to which well-assessed tools in systems theory and signal processing can be applied. In particular, after establishing the analogy between the position x in the FOM with the continuous time variable in dynamical systems, we can study the input-output response of the FOM to such infinitesimal temperature variations by applying the Laplace transform [33] to its equations and deriving the transfer function $G(s)$ from its input $I_{bb}(s)$ to its output $I_{tot}(s)$, where s is the Laplace variable:

$$G(s) \doteq \frac{I_{tot}(s)}{I_{bb}(s)} = C\left(s\mathbf{I} - A(\overline{T},\overline{p},\overline{y})\right)^{-1} B(\overline{T},\overline{p},\overline{y}), \quad (14)$$

In (14), A, B are the matrices given in equation (11) and evaluated at the chosen temperature, pressure and composition values, $\mathbf{I}$ is the identity matrix of suitable order and $(s\mathbf{I} - A)^{-1}$ denotes a matrix inverse operation. A tool commonly used to analyze the transfer function of a dynamical system is the Bode diagram of the corresponding frequency response, obtained by evaluating the magnitude and phase of $G(j\omega)$, where $\omega = \frac{2\pi}{\tau}$ assumes here the physical meaning of the frequency of purely sinusoidal oscillations (in space) of the black-body intensity (i.e. of temperature), with infinitesimal amplitude, with the period τ measured in m (e.g. $\omega = 628\,\text{rad/m}$ corresponds to a period of oscillation of the input of roughly $10^{-2}\,\text{m}$). As an example, the Bode diagram of the FOM frequency response obtained by fixing $\overline{T} = 16,300\,\text{K}$, $\overline{p} = 5\,10^5\,\text{Pa}$ and $\overline{y}$ containing 50% silver, 25% air and 25% hydrogen (whose absorption spectrum is shown in Figure 4) is shown in Figure 8. It can be noted that the overall behavior of the FOM is that

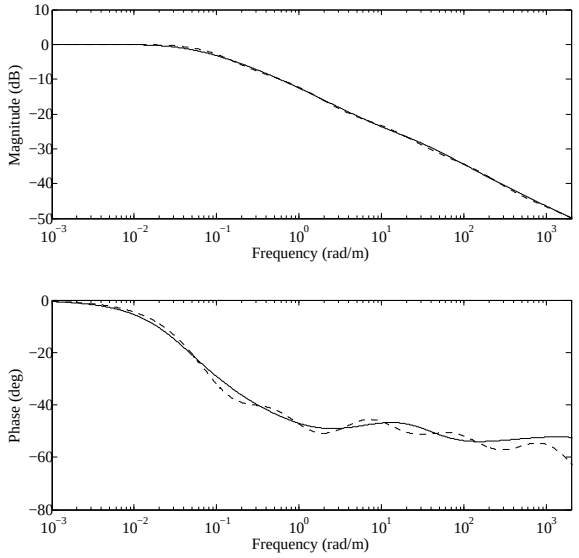

Fig. 8. Example of frequency response for a mixture of 50% silver, 25% air and 25% hydrogen at 16,300 K and 10^5 Pa. Solid: full-order model; dashed: reduced-order model with $M = 5$ bands.

of a low-pass filter, whose frequency response is shaped by the contributions of the large number of internal states present in the system. As a quantitative example regarding this case, a sinusoidal oscillation of the black-body intensity (due to an oscillation in temperature) with a period of $2\pi\,10^3\,\text{m}$ would give rise, in the gaseous medium, to a sinusoidal distribution of radiated heat intensity with unchanged amplitude and phase with respect to what would happen in vacuum (compare Figure 8 with $\omega = 10^{-3}\,\text{rad/m}$), i.e. the amplitude of the oscillations would be equal to that of the input black-body intensity, and the spatial distribution would show almost zero phase shift. On the other hand, the spatial distribution of radiated heat induced by a sinusoidal oscillation of the black-body intensity with a period of 2π m (compare again Figure 8, with $\omega = 1\,\text{rad/m}$) would have an amplitude equal to only about 23% with respect to that of the input, with a phase lag of about $45\,\text{deg}$.

If we consider now the order reduction of such a dynamical system, we see that this is a standard problem of model order reduction of LPI systems, for which a well-established literature exist, see e.g. [23], [1]. Thus, we can use one of the existing approaches to derive a reduced-order model that approximates the FOM for the chosen values of $\overline{T}, \overline{p}$ and $\overline{y}$. After deriving the ROM, the related transfer function can be computed as (compare equation (13)):

$$\hat{G}(s) \doteq \frac{\hat{I}_{tot}(s)}{\overline{I}_{bb}(s)} = \hat{C}\left(s\mathbf{I} - \hat{A}(\overline{T},\overline{p},\overline{y})\right)^{-1} \hat{B}(\overline{T},\overline{p},\overline{y}). \quad (15)$$

A comparison between the Bode diagram of the latter and that of the FOM reveals that up to very small gain values of about 10^{-4}, such that the corresponding radiated heat intensity is negligible, the frequency responses of the two models are practically super-imposed, hence indicating a very good agreement between them. Moreover, applying this procedure for many values of $\overline{T}, \overline{p}$ and $\overline{y}$, chosen by gridding their respective domains $\mathcal{T}$, $\mathcal{P}$ and $\mathcal{Y}$, shows that such a good agreement is obtained always with no more than four-five bands in the ROM. A good agreement up to a gain of about 5% is obtained with just two bands in the ROM, for oscillation periods of fractions of millimeters. Indeed, this level of accuracy would be enough for the sake of arc plasma CFD simulations, where the resolution of the spatial discretization of the considered volume is of the order of $10^{-3}\,\text{m}$. An example of the obtained results is depicted in Figure 8, too. In particular, the ROM whose frequency response is shown in the figure has five bands, $\mu_1, \ldots, \mu_5$, and the corresponding absorption coefficients and emissivities (and frequency boundaries) are equal to

$$\begin{aligned}
\hat{\alpha}(\overline{T},\overline{p},\overline{y},\mu_1) &= 1.1\,10^{-1}\ \text{m}^{-1}\\
\hat{\alpha}(\overline{T},\overline{p},\overline{y},\mu_2) &= 9.2\,10^{-1}\ \text{m}^{-1}\\
\hat{\alpha}(\overline{T},\overline{p},\overline{y},\mu_3) &= 1.3\,10^{1}\ \text{m}^{-1}\\
\hat{\alpha}(\overline{T},\overline{p},\overline{y},\mu_4) &= 1.2\,10^{2}\ \text{m}^{-1}\\
\hat{\alpha}(\overline{T},\overline{p},\overline{y},\mu_5) &= 1.7\,10^{3}\ \text{m}^{-1}\\
\hat{e}(\overline{T},\overline{p},\overline{y},\mu_1) &= 7.2\ 10^{-1}\ \ [0,\ 1.6\,10^{15}]\,\text{Hz}\\
\hat{e}(\overline{T},\overline{p},\overline{y},\mu_2) &= 2.1\ 10^{-1}\ \ (1.6\,10^{15},\ 2.4\,10^{15}]\,\text{Hz}\\
\hat{e}(\overline{T},\overline{p},\overline{y},\mu_3) &= 5.4\ 10^{-2}\ \ (2.4\,10^{15},\ 3.1\,10^{15}]\,\text{Hz}\\
\hat{e}(\overline{T},\overline{p},\overline{y},\mu_4) &= 1.2\ 10^{-2}\ \ (3.1\,10^{15},\ 3.8\,10^{15}]\,\text{Hz}\\
\hat{e}(\overline{T},\overline{p},\overline{y},\mu_5) &= 3.9\ 10^{-3}\ \ (3.8\,10^{15},\ +\infty)\,\text{Hz}
\end{aligned}$$

A comparison between these values and Figure 8 shows that the values of the ROM absorption coefficients correspond to the dominant poles of the FOM, as the intuition would suggest.

Overall, the analysis reported so far provides if not a rigorous proof at least an indication that the problem we are dealing with has a reasonable solution, using ROMs of quite low order. In Section III, we describe in details the solution

approach that we propose to deal with the linear-parameter-varying case.

C. Position discretization

Before proceeding further, it is convenient to introduce the discretized versions of the FOM and of the ROM, where the position variable x is taken at nodes x_l, $l \in \mathbb{N}$, that are equally spaced by an interval Δx. The latter has to be chosen according to the features of the problem at hand, trading off computational speed with a sufficiently fine discretization, which can capture well the fastest transients of the model's input and output. As a rule of thumb, $\Delta x \simeq \delta/10$ can be chosen, where δ is the smallest space-scale of interest in the problem (typically in our case $\delta \simeq 10^{-3}$ m, as mentioned above). Hence, all the space-dependent variables (i.e. T, p, y) are now evaluated at discrete position values. The discretization of the radiation models is carried out by assuming that such variables are constant between two subsequent position nodes, x_l and $x_{l+1} = x_l + \Delta x$, and then computing the explicit integration of (10) (for the FOM) and (12) (for the ROM). In particular, for the full-order model we have:

$$\begin{aligned} \overline{I}(x_{l+1}) &= A_d(T(x_l), p(x_l), y(x_l))\, \overline{I}(x_l) \\ &\quad + B_d(T(x_l), p(x_l), y(x_l))\, \overline{I}_{bb}(T(x_l)) \\ I_{tot}(x_l) &= C\, \overline{I}(x_l) \end{aligned} \tag{16}$$

where the matrices A_d and B_d are computed as:

$$\begin{aligned} A_d(T,p,y) &\doteq \mathrm{diag}([a(T,p,y,\nu_1), \\ &\quad \ldots, a(T,p,y,\nu_N)]^\top) \in \mathbb{R}^{N\times N} \\ \hat{B}_d(T,p,y) &\doteq [(1-a(T,p,y,\nu_1))e(T,\nu_1), \\ &\quad \ldots, (1-a(T,p,y,\nu_N))e(T,\nu_N)]^\top \in \mathbb{R}^{N\times 1} \end{aligned} \tag{17}$$

and

$$a(T,p,y,\nu_i) = e^{-\alpha(T,p,y,\nu_i)\Delta x},\ i = 1,\ldots,M.$$

The matrix C in (16) is the same as in (10), since the output equation is static and thus it is not changed by the discretization of the position x. Similarly, for the reduced-order model we have:

$$\begin{aligned} \hat{\overline{I}}(x_{l+1}) &= \hat{A}_d(T(x_l), p(x_l), y(x_l))\, \hat{\overline{I}}(x_l) \\ &\quad + \hat{B}_d(T(x_l), p(x_l), y(x_l))\, \overline{I}_{bb}(T(x_l)) \\ \hat{I}_{tot}(x_l) &= \hat{C}\, \hat{\overline{I}}(x_l) \end{aligned} \tag{18}$$

where the matrices $\hat{A}_d$ and $\hat{B}_d$ are computed as:

$$\begin{aligned} \hat{A}_d(T,p,y) &\doteq \mathrm{diag}([\hat{a}(T,p,y,\mu_1), \\ &\quad \ldots, \hat{a}(T,p,y,\mu_M)]^\top) \in \mathbb{R}^{M\times M} \\ \hat{B}_d(T,p,y) &\doteq [(1-\hat{a}(T,p,y,\mu_1))\hat{e}(T,p,y,\mu_1), \\ &\quad \ldots, (1-\hat{a}(T,p,y,\mu_M))\hat{e}(T,p,y,\mu_M)]^\top \\ &\quad \in \mathbb{R}^{M\times 1} \end{aligned} \tag{19}$$

and

$$\hat{a}(T,p,y,\mu_i) = e^{-\hat{\alpha}(T,p,y,\mu_i)\Delta x},\ i = 1,\ldots,M. \tag{20}$$

Also for the ROM the matrix $\hat{C}$ in (18) is the same as in (12).

The reason why we employ such a space discretization is twofold: on the one hand, it is needed to obtain a finite-dimensional computational problem, on the other hand it improves the computational efficiency of the method (in particular by using a constant discretization step Δx).

III. Model order reduction of the radiative heat transfer equation

A. Solution approach

Considering the analysis of Section II-B, one can be tempted to derive the ROM, i.e. the functions $\hat{\alpha}(T,p,y)$ and $\hat{e}(T,p,y)$, by gridding the domains $\mathcal{T}, \mathcal{P}$ and $\mathcal{D}$ and for each triplet $(\overline{T}, \overline{p}, \overline{y})$ compute the equivalent absorption coefficient and emissivity of the corresponding LPI model, using well-assessed and efficient model order reduction techniques. Then, the ROM could be obtained by interpolating among the computed reduced-order LPI models. This approach could work well if only pressure and composition dependence were considered, since the sensitivity of the base data on these values is mild and hence one can be confident that interpolating among the bands computed at different triplets yields correct results. In other words, for a given temperature $\overline{T}$, the absorption spectrum of the FOM does not change dramatically between two neighboring pairs $(\overline{p}_1, \overline{y}_1)$ and $(\overline{p}_2, \overline{y}_2)$ within the pressure and composition intervals of interest for the application considered here, so that for each band μ_i of the ROM it is safe to interpolate between the coefficients $\hat{\alpha}(\overline{T}, \overline{p}_1, \overline{y}_1, \mu_i)$ and $\hat{\alpha}(\overline{T}, \overline{p}_2, \overline{y}_2, \mu_i)$, computed independently by means of LPI model order reduction, to obtain the ROM coefficients for generic values of $(\overline{T}, p, y)$ with $p \in [\overline{p}_1, \overline{p}_2]$, $y \in [\overline{y}_1, \overline{y}_2]$. However, this procedure would not achieve good results when temperature dependence is taken into account as well. In fact, the dependence of the absorption spectrum on temperature is very strong (compare Figure 5), so that the ROM coefficients pertaining to the same band (e.g. μ_1) but computed at two different temperature values, even with the same pressure and composition values, might be completely unrelated to each other, and interpolating between them can give highly inaccurate results. Driven by these considerations, we adopt a hybrid strategy, where we grid the domains $\mathcal{P}$ and $\mathcal{Y}$ and for each pair $(\overline{p}, \overline{y})$ we derive the partition of the EM spectrum in M bands and the related functions $\hat{\alpha}(T, \overline{p}, \overline{y}, \mu_i)$, $i = 1, \ldots, M$ that define the ROM. Since the corresponding FOM is now parameter varying (because we let the temperature distribution change while fixing only pressure and composition), this problem falls in the class of model-order reduction of LPV systems, for which, differently from the LPI case, few results exist in the literature [37], [32], and their practical applicability to systems with $\approx 10^5$ states, like the FOM in our problem, is not straightforward. For the above reasoning, in the remainder of this section it is assumed, unless otherwise stated, that a fixed pair $(\overline{p}, \overline{y})$ of pressure and composition values has been chosen, and that the only space-varying variable is the temperature T. The complete ROM can be then obtained by repeating the LPV order-reduction for all the pairs $(\overline{p}, \overline{y})$ chosen by gridding the respective domains, and then interpolating among the obtained values to compute the equivalent absorption coefficients and frequency bands for a generic triplet (T, p, y).

Remark 1: The simplification introduced by fixing pressure and composition is made possible thanks to the above-discussed particular properties of the absorption spectra of the considered gaseous media. Indeed, such a simplification by itself is not required for the order-reduction technique described in the following, which may straightforwardly be applied also with varying pressure and composition, but at the

price of higher computational requirements. In our experience, using constant pressure and composition in the order reduction computation yields accurate enough results for the applications of interest.

In the following, we propose to address the LPV order reduction problem with a nonlinear system identification approach (see e.g. [24]), in which we search, within a given set of possible ROMs, the one which is closest to the FOM according to a pre-defined optimality criterion. In the next sections, this task is brought in the form of a tractable optimization program. It has to be noted at this point that, in the literature on system identification, there exist several contributions devoted to the problem of identification of LPV systems, see e.g. [5] and the references therein. However, such results are not applicable in our case, due to the additional constraints that are present on the ROM, namely the need to preserve a specific structure where the total radiated intensity is the sum of the contributions given by the frequency bands. Differently from such previous approaches, the one proposed here is able to take into account these constraints, since it is specifically tailored for the considered application.

B. Cost function, model set, and formulation of the optimization problem

In order to have an optimization problem that can be solved with common numerical techniques, two main ingredients need to be defined: the set of reduced-order models of the form (18) where we carry out our search, denoted with $\mathcal{H}$ (model set), and a cost function J giving a measure of how much a given ROM $H \in \mathcal{H}$ is close to the FOM. The model set $\mathcal{H}$ should represent the limitations that we want to impose on the ROM in order to account for the physics of the problem. A ROM is fully characterized by its parameters $\hat{\alpha}(T, \overline{p}, \overline{y}, \mu_i)$, $\hat{e}(T, \overline{p}, \overline{y}, \mu_i)$, $i = 1, \dots, M$, which in the considered settings are, for each band μ_i, functions of temperature only. To be consistent with the underlying physical phenomena, the equivalent absorption coefficients should be positive (to retain an asymptotically stable model):

$$\hat{\alpha}(T, \overline{p}, \overline{y}, \mu_i) > 0, \, \forall T \in \mathcal{T}, \, i = 1, \dots, M \tag{21}$$

and the equivalent emissivities should lie in the interval $[0, \, 1]$ and sum to one over all the considered temperature range, in analogy with (8), so that the black-body limit is not violated:

$$\begin{aligned} &0 \leq \hat{e}(T, \overline{p}, \overline{y}, \mu_i) \leq 1, \, \forall T \in \mathcal{T}, \, i = 1, \dots, M \\ &\sum_{i=1}^{M} \hat{e}(T, \overline{p}, \overline{y}, \mu_i) = 1, \, \forall T \in \mathcal{T} \end{aligned} \tag{22}$$

Since equation (20) is invertible, we can equivalently consider the functions $\hat{a}(T, \overline{p}, \overline{y}, \mu)$ to define the model set. We select this alternative for the sake of computational efficiency, as we will discuss more in details in Section III-C3. Then, the constraints (21) can be re-written as:

$$0 \leq \hat{a}(T, \overline{p}, \overline{y}, \mu_i) < 1, \, \forall T \in \mathcal{T}, \, i = 1, \dots, M \tag{23}$$

As a final step to define $\mathcal{H}$, we choose a finite parametrization of functions $\hat{a}(T, \overline{p}, \overline{y}, \mu_i)$ and $\hat{e}(T, \overline{p}, \overline{y}, \mu_i)$, in order to obtain a finite dimensional model set (hence also a finite dimensional optimization problem):

$$\begin{aligned} &\hat{a}(T, \overline{p}, \overline{y}, \mu) = f_{\hat{a}}(T, \theta_{\hat{a}}(\overline{p}, \overline{y}, \mu)), \, \theta_{\hat{a}}(\overline{p}, \overline{y}, \mu) \in \mathbb{R}^{n_{\theta_{\hat{a}}} \times 1} \\ &\hat{e}(T, \overline{p}, \overline{y}, \mu) = f_{\hat{e}}(T, \theta_{\hat{e}}(\overline{p}, \overline{y}, \mu)), \, \theta_{\hat{e}}(\overline{p}, \overline{y}, \mu) \in \mathbb{R}^{n_{\theta_{\hat{e}}} \times 1} \end{aligned}, \tag{24}$$

where $f_{\hat{a}}$, $f_{\hat{e}}$ are chosen, once again, to tradeoff the flexibility of the parametrization with computational efficiency, and $n_{\theta_{\hat{a}}}, \, n_{\theta_{\hat{e}}} \in \mathbb{N}$ are the numbers of free parameters in such functions. In particular, a convenient choice for $f_{\hat{a}}$ is the class of piecewise affine functions of temperature, while $f_{\hat{e}}$ is taken such that the corresponding parameters $\theta_{\hat{e}}$ define the partitioning of the EM spectrum in a finite number M of bands. These choices have the advantage of yielding a convex model set (see Section III-C2 for details), hence improving the computational efficiency and stability of the procedure. For a given pair $(\overline{p}, \overline{y})$, let us collect the parameters $\theta_{\hat{a}}$ and $\theta_{\hat{e}}$ for all the ROM bands μ_i in a single vector θ:

$$\theta \doteq \begin{bmatrix} \theta_{\hat{a}}(\overline{p}, \overline{y}, \mu_1) \\ \vdots \\ \theta_{\hat{a}}(\overline{p}, \overline{y}, \mu_M) \\ \theta_{\hat{e}}(\overline{p}, \overline{y}, \mu_1) \\ \vdots \\ \theta_{\hat{e}}(\overline{p}, \overline{y}, \mu_M) \end{bmatrix} \in \mathbb{R}^{n_\theta \times 1}, \tag{25}$$

where $n_\theta = M(n_{\theta_{\hat{a}}} + n_{\theta_{\hat{e}}})$ is the total number of optimization variables. Then, considering (22)-(25), we can define the model set $\mathcal{H}$ as

$$\mathcal{H} \doteq \left\{ \theta \in \mathbb{R}^{n_\theta \times 1} : \begin{array}{c} 0 \leq f_{\hat{a}}(T, \theta_{\hat{a}}(\overline{p}, \overline{y}, \mu_i)) < 1, \, i = 1, \dots, M \\ 0 \leq f_{\hat{e}}(T, \theta_{\hat{e}}(\overline{p}, \overline{y}, \mu_i)) \leq 1, \, i = 1, \dots, M \\ \sum_{i=1}^{M} f_{\hat{e}}(T, \theta_{\hat{e}}(\overline{p}, \overline{y}, \mu_i)) = 1 \\ \forall T \in \mathcal{T} \end{array} \right\}, \tag{26}$$

As to the cost function J, this should represent a criterion by which the accuracy of the ROM is evaluated. As discussed in Section II, an indicator of the accuracy of a ROM, suitable for the considered application, is related to the error between its total output intensity profile and that of the FOM, given the same temperature profile. Motivated by this consideration, we select a series of temperature profiles, and then evaluate the discrepancy between the corresponding outputs generated by the FOM and those given by the ROM. More specifically, let us consider a space interval $X = [0, \overline{x}]$, chosen such that $\overline{x} = (L-1)\,\Delta x$ for some $L \in \mathbb{N}$. Similarly to the choice of Δx, the value of $\overline{x}$ depends on the problem at hand: a typical choice is three-four times the largest space-scale of interest (see Section III-C1 for details). Thus, in the interval X we have L position nodes x_l, $l = 1, \dots, L$, with $x_1 = 0$ and $x_L = \overline{x}$. Consider now a finite sequence of $L_T \in \mathbb{N}$ discretized temperature profiles $\tilde{T}_j \doteq [T_j(x_1), \dots, T_j(x_L)]^\top \in \mathbb{R}^{L \times 1}$, $j = 1, \dots, L_T$. In face of each of such temperature profiles, the FOM provides a corresponding profile of the radiated intensity, $\tilde{I}_{tot,j}(\tilde{T}_j) \doteq [I_{tot,j}(x_1), \dots, I_{tot,j}(x_L)]^\top \in \mathbb{R}^{L \times 1}$, $j = 1, \dots, L_T$, and similarly the ROM, for a given value of θ provides an approximated one, $\tilde{\hat{I}}_{tot,j}(\tilde{T}_j, \theta)$. Let us define the weighted error profile as

$$\begin{aligned} \Delta I_j(\theta) \doteq \; & \left[w_j(\tilde{I}_{tot,j}(\tilde{T}_j) - \tilde{\hat{I}}_{tot,j}(\tilde{T}_j, \theta)) \right]^\top \in \mathbb{R}^{L \times 1}, \\ & j = 1, \dots, L_T, \end{aligned} \tag{27}$$

where $w_j > 0$ is a scalar weight (the specific choice of w_j is discussed in Section III-C1). Then, we take the cost function as:

$$J(\theta) = \sum_{j=1}^{L_T} \Delta I_j^\top(\theta) \Delta I_j(\theta), \tag{28}$$

i.e. the sum, over all error profiles and over all position nodes of each profile, of the weighted intensity error squared.

Remark 2: As an alternative cost function, one can also employ the discrepancy between the divergence of the radiated heat computed with the FOM and with the ROM. Such a quantity is related to the distribution of heat inside the plasma volume, while the propagated intensity (which we use for our computations) is related to the heat transferred to the walls. More in general, one can employ a multi-objective cost given by a weighted sum of the two quantities; this can be done straightforwardly in our approach. Given that the initial condition at the boundary is fixed, in principle fitting one or the other quantity should be equivalent, however in practice there are slight differences in the obtained coefficients. In our experience, the use of the radiated heat intensity gives better results, therefore we consider this cost function here.

We can now write the model order reduction problem in a computationally tractable form:

$$\min_{\theta \in \mathcal{H}} J(\theta) \tag{29}$$

where $\mathcal{H}$ and $J(\theta)$ are given in (26) and (28), respectively. Namely, the aim of the optimization problem (29) is to search, within the model set $\mathcal{H}$, the value of the parameter vector θ that achieves the best fitting criterion $J(\theta)$. Problem (29) is a finite-dimensional nonlinear program (NLP) which, for a suitable choice of the model parametrization (24), can be tackled with state-of-the-art numerical methods [25]. As we show in the examples of Section IV, a typical dimension of the optimization variable is $n_\theta \approx 77$, corresponding for example to a 3rd-order model with 25 parameters defining the functions $\hat{a}(T, \overline{p}, \overline{y}, \mu_i)$ and two parameters defining the frequency cuts in the EM spectrum that separate the three bands μ_1, μ_2, μ_3. In general, the cost function (28) is non-convex with respect to the decision variable θ, so that only a local solution to problem (29) can be computed efficiently with such problem dimensions. As we show in the examples of Section (IV), the obtained solutions nevertheless yield ROMs that are very accurate with respect to the FOM.

In the next section, we discuss several aspects involved in the formulation and solution of (29), including the design of the input temperature profiles and the choice of the weights in the cost function J (28), the choice of model parametrization, the numerical approach to solve the NLP, finally some ways to improve the efficiency and stability of the numerical optimization.

C. Computational aspects

1) Input design, weighting coefficients and initial conditions: From an application's perspective, the position interval $\overline{x}$, the resolution of the position discretization Δx, and the temperature profiles $\tilde{T}_j$, $j = 1, \ldots, L_T$ should be representative of the typical temperature distributions in the plasma that is generated during the switching process. About the choice of Δx, considering the discussion in Section II-C, a reasonable tradeoff between accuracy and computational speed is $\Delta x = 10^{-4}$ m, while for $\overline{x}$ a good choice in our experience is $\overline{x} = 2\,10^{-1}$ m, for arcs whose width is between $\approx 3\,10^{-3}$ m and $\approx 2\,10^{-2}$ m, corresponding to current values in the range 1-40 10^3 A. Finally, for the temperature profiles, we select a bell-shaped function, where we can adjust the maximum temperature reached as well as the steepness of the rising and falling slopes. Then, we generate a series of such profiles by cycling through different maximum temperatures and transient slopes. Furthermore, from a system identification's perspective, given the nonlinearity of the system's equations, different initial conditions for the internal states of the model should be considered, and the input should be designed in order to excite the system in a broad range of frequencies. For the former aspect, we replicate the temperature profile several times, so that the system is presented more than once with the same temperature profile, but each time starting from the internal states resulting from the previous profile. For the second aspect, white noise processes are a well-known choice [20] to excite the system's dynamics over all frequencies, hence we super-impose to the computed profiles a uniformly distributed white noise temperature signal whose amplitude is a fraction (e.g. 25%) of the highest temperature in the original profile. With these choices, typical temperature profiles are shown in Figure 9(a)-(b), together with the resulting intensity distributions computed with the FOM for a mixture of pure air.

Due to the fourth-order dependence of the total black-body intensity on temperature (see (4)), the radiated intensity obtained with different temperature profiles can have different orders of magnitude, compare for example Figure 9(a) with Figure 9(b), where the maximum temperatures are about 10^4 K and $1.7\ 10^4$ K, respectively. If no corrective measure is taken, such a difference among the various intensity profiles would lead to poor accuracy of the reduced-order models, due to the biasing towards the higher intensity values in the cost function. In order to compensate this effect, we select the weights w_j in (27) on the basis of the radiated heat intensity given by the FOM when the corresponding temperature profile, $\tilde{T}_j$, is considered. In this way, all the error profiles (27) are normalized with respect to the corresponding intensity; typical specific choices for the weights include the reciprocal of the maximum or of the average radiated heat, i.e.:

$$w_j = \frac{1}{\max(\tilde{I}_{tot,j}),\ j = 1, \ldots, L_T}$$

or

$$w_j = \frac{1}{\text{mean}(\tilde{I}_{tot,j}),\ j = 1, \ldots, L_T}$$

Finally, it is worth mentioning the choice of the initial conditions for the radiated heat intensity, for both the FOM and the ROM, i.e. the values of vectors $\overline{I}(x_1)$ and $\hat{\overline{I}}(x_1)$ needed to simulate the models (16) and (18), respectively, in the interval $X = [0, \overline{x}]$. To this end, we assume that for $x < 0$ (i.e. outside such an interval) the incoming radiation in positive x direction corresponds to the steady-state intensity at ambient temperature T_a, i.e. $I_{bb}(T_a, \nu_i)$, $i = 1, \ldots, N$ for the FOM and

$$\hat{I}_j(x_1, \mu_i) = \hat{e}(T_a, \overline{p}, \overline{y}, \mu_i) \overline{I}_{bb}(T_a),\ i = 1, \ldots, M \tag{30}$$

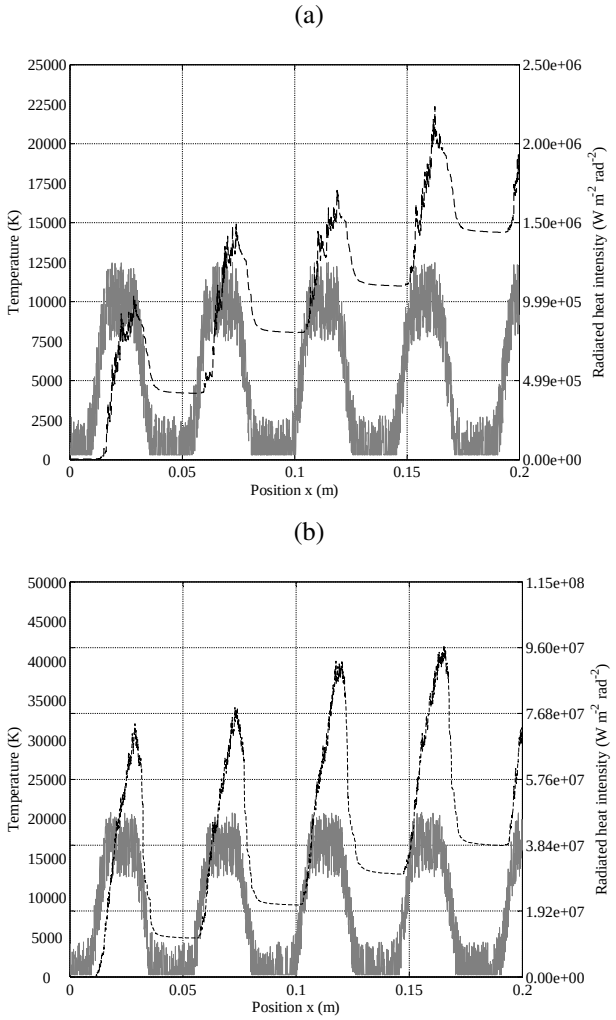

Fig. 9. Example of input temperature profiles used in the order reduction procedure (solid gray lines) and radiated heat intensity distribution computed with the full-order model (dashed black lines). The maximum temperature values prior to adding white noise are (a) 10^4 K and (b) $1.7\ 10^4$ K . Base data: pure air at $1.5\,10^5$ Pa.

for the ROM. The rationale behind this choice is that in the arc simulations related to switchgear devices one can assume that initially the boundaries of the computational domain are at ambient temperature and radiate the corresponding intensity into the volume filled with plasma. Additionally, the boundaries can not reach temperatures higher than about 3,000 K (depending on the material), such that the related radiated heat is anyway negligible with respect to the intensity emitted in the plasma volume where current is flowing.

2) Model parametrization and model set: The choice of the model parametrization, i.e. of functions $f_{\hat{a}}$ and $f_{\hat{e}}$ in (24), is crucially important for the accuracy of the obtained results and for the solution of the numerical optimization. For the first aspect, one shall choose a rich enough family of functions, such that the data from the FOM can be reproduced with small errors. For the second aspect, the best choice would be a parametrization leading to a convex model set (26), so that sequential quadratic programming and line search algorithms [25] can be used efficiently. For the equivalent absorption coefficients $\hat{a}$, i.e. function $f_{\hat{a}}$, a choice that meets both requirements is a piecewise affine parametrization, where $\theta_{\hat{a}}(\overline{p},\overline{y},\mu_i)$ is, for each band $i=1,\dots,M$, a vector containing the values of the coefficients $\hat{a}$ at a finite number of predefined temperature nodes T_k, $k=1,\dots,N_k$, such that $T_{k-1}<T_k$, $k=2,\dots,N_k$, chosen by the user (e.g. equally spaced):

$$\theta_{\hat{a}}(\overline{p},\overline{y},\mu_i)=\begin{bmatrix}\theta_{\hat{a}}(T_1,\overline{p},\overline{y},\mu_i)\\ \vdots \\ \theta_{\hat{a}}(T_{N_k},\overline{p},\overline{y},\mu_i)\end{bmatrix}\in\mathbb{R}^{N_k\times 1},\quad i=1,\dots,M.$$

The temperature nodes must include the values at the boundaries (1) of the domain $\mathcal{T}$, i.e. $T_1=T_{\min}$ and $T_{N_k}=T_{\max}$. Then, for a given temperature value $T\in\mathcal{T}$, the function $f_{\hat{a}}$ in (24) is computed by interpolating linearly among the values of $\theta_{\hat{a}}$ corresponding to the neighboring temperature nodes:

$$f_{\hat{a}}(T,\theta_{\hat{a}}(\overline{p},\overline{y},\mu_i))=\lambda(T)^\top\theta_{\hat{a}}(\overline{p},\overline{y},\mu_i), \tag{31}$$

where

$$\lambda(T)=\begin{bmatrix}0\\ \vdots \\ 1-\dfrac{T-T_{k-1}}{T_k-T_{k-1}}\\ \dfrac{T-T_{k-1}}{T_k-T_{k-1}}\\ \vdots \\ 0\end{bmatrix}\in\mathbb{R}^{N_k\times 1} \tag{32}$$

and T_{k-1}, T_k are two subsequent nodes such that $T\in[T_{k-1},T_k]$. Using the parametrization (31), the number of optimization variables introduced in the problem is $M\,N_k$. The flexibility of the approximating function $f_{\hat{a}}$ can be increased by increasing the number of temperature nodes N_k. Moreover, note that $f_{\hat{a}}$ in (31) is a convex combination [11] of the elements contained in the parameter vector. Therefore, with this parametrization, the constraints (23) can be enforced by imposing them just on the values at the nodes, i.e.:

$$0\le\hat{a}(T_k,\overline{p},\overline{y},\mu_i)<1,\ k=1,\dots,N_k,\ i=1,\dots,M\ . \tag{33}$$

As regards the parametrization of the equivalent emissivity functions, $\hat{e}(T,\overline{p},\overline{y},\mu_i)$, an additional requirement is to retain a physical link between the emissivities of each band in the ROM and the original absorption spectrum, such that each μ_i accounts for the intensity contributed by a precise frequency interval defined by suitable frequency cuts. As already mentioned, previous contributions in the literature actually consider such a partitioning of the EM spectrum [26], [19], however the choice of the frequency bands is not trivial and not systematic, so that one has to proceed with a trial-and-error approach. With the technique proposed here, one can optimize directly with respect to such frequency cuts, hence obtaining a systematic method for the band-averaging. This can be done by using the following model parametrization for the equivalent emissivities:

$$\begin{aligned}f_{\hat{e}}(T,\theta_{\hat{e}}(\overline{p},\overline{y},\mu_i))&=\gamma(T,\theta_{\hat{e}}(\overline{p},\overline{y},\mu_i))\\ &\doteq\int_{\theta_{\hat{e}_{hf}}(\overline{p},\overline{y},\mu_{i-1})}^{\theta_{\hat{e}_{hf}}(\overline{p},\overline{y},\mu_i)}e(T,\nu)d\nu,\end{aligned} \tag{34}$$

where $e(T,\nu)$ is the spectral emissivity (8) and the optimization variables are the upper boundaries (e.g. in Hz) of each frequency band:

$$\theta_{\hat{e}}(\overline{p},\overline{y},\mu_i) = \left[\begin{array}{c} \theta_{\hat{e}_{hf}}(\overline{p},\overline{y},\mu_1) \\ \vdots \\ \theta_{\hat{e}_{hf}}(\overline{p},\overline{y},\mu_{M-1}) \end{array}\right] \in \mathbb{R}^{(M-1)\times 1}.$$

For the first and last bands, i.e. μ_1 and μ_M, the equivalent emissivity is computed using (34) with $\theta_{\hat{e}_{hf}}(\overline{p},\overline{y},\mu_0) \rightarrow 0$ and $\theta_{\hat{e}_{hf}}(\overline{p},\overline{y},\mu_M) = +\infty$, respectively. In this way, the equivalent emissivity of each band is, by construction, equal to the one pertaining to the frequency interval $[\theta_{\hat{e}_{hf}}(\overline{p},\overline{y},\mu_{i-1}),\, \theta_{\hat{e}_{hf}}(\overline{p},\overline{y},\mu_i)]$. The constraints (22) defining the model set (i.e. the second and third rows in (26)) can be easily taken into account by a set of linear inequalities:

$$\begin{array}{l} \theta_{hf}(\overline{p},\overline{y},\mu_1) > 0 \\ \theta_{hf}(\overline{p},\overline{y},\mu_{i+1}) > \theta_{hf}(\overline{p},\overline{y},\mu_i),\; i = 2,\ldots,M-2 \end{array} . \quad (35)$$

The constraints (35) impose an increasing ordering of the boundaries. By construction, the resulting bands are not overlapping and they cover the whole spectrum: these features automatically enforce the constraints (22). We note that with this parametrization, the number of free variables that define the band partition is equal to $M-1$. Therefore, considering also the parameters pertaining to the equivalent absorption coefficients, the total number of optimization variables in the problem is equal to $M\,N_k + M - 1$. About the total number of constraints, in virtue of (33) we have a set of $2\,M\,N_k$ linear inequalities, while (35) amounts to $M-1$ additional inequalities, for a total of $2\,M\,N_k + M - 1$. These inequalities altogether define indeed a convex set (in particular a polytope) where the solution of the optimization problem is confined.

About the computation of $\gamma(T,\theta_{\hat{e}}(\overline{p},\overline{y},\mu_i))$ in (34), note that this function can be also written as:

$$\begin{array}{l} \gamma(T,\theta_{\hat{e}}(\overline{p},\overline{y},\mu_i)) \\ = f_\gamma(T,\theta_{\hat{e}_{hf}}(\overline{p},\overline{y},\mu_i)) - f_\gamma(T,\theta_{\hat{e}_{hf}}(\overline{p},\overline{y},\mu_{i-1})) \end{array} \quad (36)$$

where

$$f_\gamma(T,\theta) \doteq \int_0^\theta e(T,\nu)d\nu. \quad (37)$$

The function $f_\gamma : \mathcal{T} \times \mathbb{R}^+ \rightarrow [0,1]$ can be conveniently pre-computed and stored, so that the computation of $\gamma(T,\theta_{\hat{e}}(\overline{p},\overline{y},\mu_i))$ can be very efficient.

3) NLP solution and computational aspects: After choosing the temperature profiles and the model parametrization as described in Sections III-C1 and III-C2, respectively, it can be shown that the cost function J (28) is twice differentiable. Thus, considering also the convexity of the model set, the optimization problem (29) can be solved for a local minimum with constrained sequential quadratic programming (SQP) techniques [25], like the one implemented in Matlab® function `fmincon`. The computational efficiency and stability of the numerical optimization depend on a number of aspects, which are briefly mentioned here.

Computation of the cost function. SQP solvers employ (as most NLP solution algorithms) an iterative strategy where the cost function might need to be evaluated hundreds of times. It is thus imperative to speed-up the computation of such a function which, in our case, implies the computation of the $L-$dimensional vectors $\Delta I_j(\theta) = w_j(\tilde{I}_{tot,j}(\tilde{T}_j) - \hat{\tilde{I}}_{tot,j}(\tilde{T}_j,\theta))$, $j = 1,\ldots,L_T$, see (27)-(28). The intensity profiles given by the FOM, $\tilde{I}_{tot,j}(\tilde{T}_j)$, can be computed once and used in all the function evaluations, since they are not changing with θ. On the other hand, the intensity given by the ROM, $\hat{\tilde{I}}_{tot,j}(\tilde{T}_j,\theta)$, has to be computed iteratively during the optimization. This implies evaluating the selected functions (24) and simulating the ROM model. As mentioned briefly in Section II-C, the computational times of such operations improve significantly by using the discretized version of the ROM (18) and by considering the values of $\hat{a}$, instead of $\hat{\alpha}$, as optimization parameters, since one avoids the computation of the exponential in (20). The values of $\hat{\alpha}$ can be then recovered from the optimal solution by inverting such equation. Another approach to speed up the computations is to pre-compute and store the vectors $\lambda(T_j(x_i))$, $i = 1,\ldots,L$, $j = 1,\ldots,L_T$ (32) corresponding to the employed temperature profiles, which are needed to compute the piecewise affine functions $f_{\hat{a}}(T,\theta_{\hat{a}}(\overline{p},\overline{y},\mu_i))$ (31), since these vectors do not depend on the optimization variables but just on the temperature distributions $\tilde{T}_j$.

Gradient computations. Another aspect that greatly influences the efficiency (and accuracy) of the optimization algorithm is the computation of the gradients of the cost and constraint functions. While the gradient of each constraint is trivial to compute, since only linear equalities and inequalities are present (as shown in Section III-C2), the gradient of the cost is more difficult to obtain, but we show here that it can still be derived analytically. First of all, consider that:

$$J(\theta) = \sum_{j=1}^{L_T}\sum_{l=1}^{L} w_j^2(I_{tot,j}(x_l) - \hat{I}_{tot,j}(x_l,\theta))^2 \quad (38)$$

hence

$$\begin{array}{l} \nabla_\theta J(\theta) \doteq \left[\begin{array}{c} \frac{\partial J}{\partial\theta_{\hat{a},1}(\overline{p},\overline{y},\mu_1)} \\ \vdots \\ \frac{\partial J}{\partial\theta_{\hat{e},n_{\theta_{\hat{e}}}}(\overline{p},\overline{y},\mu_M)} \end{array}\right] \\ = \sum_{j=1}^{L_T}\sum_{l=1}^{L} -2\,w_j^2\left(I_{tot,j}(x_l) - \hat{I}_{tot,j}(x_l,\theta)\right)\nabla_\theta \hat{I}_{tot,j}(x_l,\theta). \end{array} \quad (39)$$

We thus focus on deriving a general expression for the gradient $\nabla_\theta \hat{I}_{tot,j}(x_l,\theta)$ of the total radiated intensity at the $l-$th position node for the $j-$th temperature profile, which can then be employed to compute the gradient of J using (39). Exploiting the second of the model equations (18) and considering the vector $\hat{C}$ in (13), we have:

$$\nabla_\theta \hat{I}_{tot,j}(x_l,\theta) = \sum_{i=1}^{M} \nabla_\theta \hat{I}_j(x_l,\mu_i,\theta), \quad (40)$$

where $\hat{I}_j(x_l,\mu_i,\theta)$ is the intensity pertaining to the band μ_i at the position step x_l when the temperature profile $\tilde{T}_j$ is considered. Moreover, by using the first of (18) together with

(19) and (24) we obtain, for each $l = 2, \dots, L$:

$$\begin{aligned}\nabla_\theta \hat{I}_j(x_l, \mu_i, \theta) &= \nabla_\theta f_{\hat{a}}(T_j(x_{l-1}), \theta_{\hat{a}}(\overline{p}, \overline{y}, \mu_i)) \\ &\quad \hat{I}_j(x_{l-1}, \mu_i, \theta) \\ &+ f_{\hat{a}}(T_j(x_{l-1}), \theta_{\hat{a}}(\overline{p}, \overline{y}, \mu_i)) \\ &\quad \nabla_\theta \hat{I}_j(x_{l-1}, \mu_i, \theta) \\ &+ (1 - f_{\hat{a}}(T_j(x_{l-1}), \theta_{\hat{a}}(\overline{p}, \overline{y}, \mu_i))) \\ &\quad \nabla_\theta f_{\hat{e}}(T_j(x_{l-1}), \theta_{\hat{e}}(\overline{p}, \overline{y}, \mu_i)) \\ &\quad \overline{I}_{bb}(T_j(x_{l-1})) \\ &- \nabla_\theta f_{\hat{a}}(T_j(x_{l-1}), \theta_{\hat{a}}(\overline{p}, \overline{y}, \mu_i)) \\ &\quad f_{\hat{e}}(T_j(x_{l-1}), \theta_{\hat{e}}(\overline{p}, \overline{y}, \mu_i))\ \overline{I}_{bb}(T_j(x_{l-1}))\end{aligned} \tag{41}$$

The gradients $\nabla_\theta f_{\hat{a}}$ and $\nabla_\theta f_{\hat{e}}$ in (41) depend on the model parametrization. For the piecewise affine function $f_{\hat{a}}$, the computation is straightforward, e.g. (from (31)):

$$\begin{aligned}&\nabla_\theta f_{\hat{a}}(T_j(x_{l-1}), \theta_{\hat{a}}(\overline{p}, \overline{y}, \mu_i))) \\ =\ &\nabla_\theta \left(\lambda(T_j(x_{l-1}))\theta_{\hat{a}}(\overline{p}, \overline{y}, \mu_i)\right) \\ =\ &\begin{bmatrix} 0 \\ \vdots \\ \lambda(T_j(x_{l-1})) \\ \vdots \\ 0 \end{bmatrix} \in \mathbb{R}^{n_\theta \times 1},\end{aligned} \tag{42}$$

where the zeros in vector $\nabla_\theta f_{\hat{a}}$ correspond to all the other parameters in vector θ but the set $\theta_{\hat{a}}(\overline{p}, \overline{y}, \mu_i)$ pertaining to the i^{th} band.

As regards function $f_{\hat{e}}$, whose parameters are the boundaries of the spectral bands, the computation of the related gradient $\nabla_\theta f_{\hat{e}}$ involves computing the derivative of function $f_\gamma(T, \theta)$ in (37), which is readily obtained as $df_\gamma(T, \theta)/d\theta = e(T, \theta)$ (8). More specifically, considering (34) and (36)-(37) we have:

$$\begin{aligned}&\nabla_\theta f_{\hat{e}}(T_j(x_{l-1}), \theta_{\hat{e}}(\overline{p}, \overline{y}, \mu_i))) \\ =\ &\nabla_\theta \gamma\left(T_j(x_{l-1}), \theta_{\hat{e}}(\overline{p}, \overline{y}, \mu_i)\right) \\ =\ &\begin{bmatrix} 0 \\ \vdots \\ -e(T_j(x_{l-1}), \theta_{\hat{e}_{hf}}(\overline{p}, \overline{y}, \mu_{i-1})) \\ e(T_j(x_{l-1}), \theta_{\hat{e}_{hf}}(\overline{p}, \overline{y}, \mu_i)) \\ \vdots \\ 0 \end{bmatrix} \in \mathbb{R}^{n_\theta \times 1},\end{aligned} \tag{43}$$

where, in a way similar to (42), the zeros in vector $\nabla_\theta f_{\hat{e}}$ correspond to all the other parameters in vector θ but the pair $\theta_{\hat{e}_{hf}}(\overline{p}, \overline{y}, \mu_{i-1})$, $\theta_{\hat{e}_{hf}}(\overline{p}, \overline{y}, \mu_i)$ pertaining to the i^{th} band. For the first and last bands, i.e. $i = 1$ and $i = M$ respectively, the gradient is computed by replacing the spectral emissivity pertaining to $\theta_{\hat{e}_{hf}}(\overline{p}, \overline{y}, \mu_{i-1})$ (resp. $\theta_{\hat{e}_{hf}}(\overline{p}, \overline{y}, \mu_i)$) with zero, since these two boundaries are not free variables, as commented above in Section III-C2.

The last ingredient needed for the gradient computation is the initialization of $\nabla_\theta \hat{I}_j(x_l, \mu_i, \theta)$ for $l = 1$, which is required in (41); this is readily done by computing the derivative of the initial conditions (30):

$$\begin{aligned}&\nabla_\theta \hat{I}_j(x_1, \mu_i, \theta) \\ &= \nabla_\theta f_{\hat{e}}(T_a, \theta_{\hat{e}}(\overline{p}, \overline{y}, \mu_i))\ \overline{I}_{bb}(T_a),\ i = 1, \dots, M,\ j = 1, \dots, L_T\end{aligned} \tag{44}$$

By using (41)-(44), one can recursively compute the values of $\nabla_\theta \hat{I}_j(x_l, \mu_i, \theta)$ for each position node x_l, each temperature profile $\tilde{T}_j$ and each band μ_i, and then use (38)-(40) to compute the gradient of the cost function. Such a recursive gradient computation can be done together with the simulation of the ROM, which is anyway needed to compute the cost function. The alternative to such an approach would be to estimate the gradient by means of numerical differentiation, e.g. finite difference approximation, which would imply computing $n_\theta + 1$ times the cost function for a single gradient estimate. This is done by default in most available optimization routines if no gradient is provided, however it is subject to numerical errors and it requires significantly more time than the exact computation derived above. Therefore, the use of (38)-(44) to compute $\nabla_\theta J(\theta)$ is both more accurate and more efficient than numerical differentiation.

Regularization and warm start. Other important issues that can arise in the numerical solution of (29) are related to the quality of the obtained optimizer and the stability of the optimization algorithm. One aspect that is relevant for the subsequent use of the derived absorption coefficients in CFD simulations is the smoothness of the obtained functions $\hat{\alpha}$ and $\hat{\theta}$ with respect to their input arguments, T, p, y, μ_i. About the temperature dependence, if piecewise affine functions are used one can penalize the variation of $\hat{\alpha}$ (or equivalently $\hat{a}$) directly in the optimization, by augmenting the cost function with a regularization term, as follows:

$$J(\theta) = \sum_{j=1}^{L_T} \Delta I_j^\top(\theta) \Delta I_j(\theta) + \beta \Delta\theta^\top \Delta\theta,$$

where

$$\Delta\theta \doteq \begin{bmatrix} \theta_{\hat{a},2}(\overline{p}, \overline{y}, \mu_1) - \theta_{\hat{a},1}(\overline{p}, \overline{y}, \mu_1) \\ \vdots \\ \theta_{\hat{a},n_{\theta_{\hat{a}}}}(\overline{p}, \overline{y}, \mu_1) - \theta_{\hat{a},n_{\theta_{\hat{a}}}-1}(\overline{p}, \overline{y}, \mu_1) \\ \vdots \\ \theta_{\hat{a},2}(\overline{p}, \overline{y}, \mu_M) - \theta_{\hat{a},1}(\overline{p}, \overline{y}, \mu_M) \\ \vdots \\ \theta_{\hat{a},n_{\theta_{\hat{a}}}}(\overline{p}, \overline{y}, \mu_M) - \theta_{\hat{a},n_{\theta_{\hat{a}}}-1}(\overline{p}, \overline{y}, \mu_M) \end{bmatrix}$$

and β is a weighting factor that can be used to tradeoff the variability of the absorption coefficients with respect to temperature with the goodness of the fitting criterion. The gradient of this modified cost can be computed with a straightforward extension of equation (39). About the smoothness with respect to p and y, recall that we assumed that several ROMs are computed independently by gridding the $\mathcal{P}$ and $\mathcal{Y}$ domains (see Section III-A). Thus, a possible way to influence the dependence of the coefficients on pressure and composition is to warm-start the optimization, by initializing the optimization parameters with the solution obtained from neighboring values of $\overline{p}, \overline{y}$. This approach usually yields good results, as we show in the next section with some examples.

IV. Results

We applied our method to compute the equivalent absorption coefficients and the partition of the EM spectrum in frequency bands for several gaseous media, ranging from pure air to mixtures of silver (or copper), air and hydrogen, and carbon dioxide and copper. As an example, Figures 10-11 show the results for pure air, using $M = 2$ bands in the ROM.

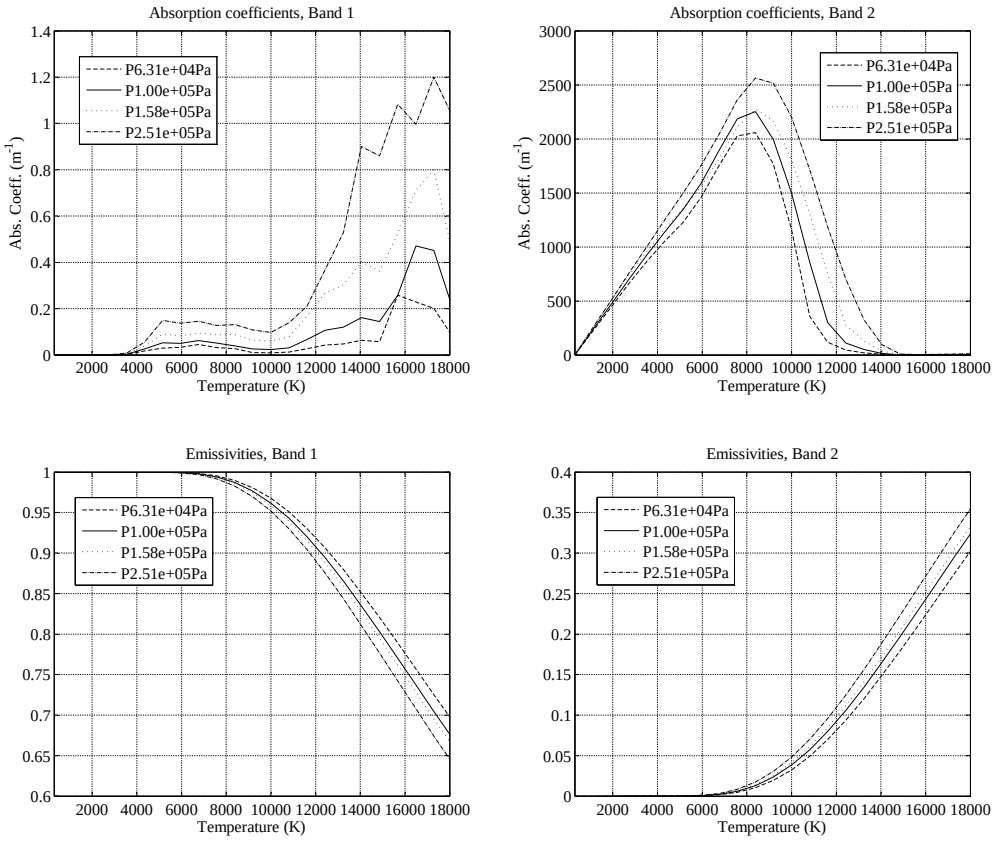

Fig. 10. Example of absorption coefficients and emissivities for a ROM with two bands for pure air.

For each temperature profile $\tilde{T}_j$, the weight w_j in (27) has been chosen by taking the reciprocal of the average value of the corresponding intensity profile computed with the FOM. From these results, it can be noted that for low pressure values (Figure 10), in a temperature range of about 12-14 10^4 K the first band accounts for more than 80% of the total black-body intensity, however with an absorption coefficient of the order of $10^{-1}\,\mathrm{m}^{-1}$. Considering that the steady-state intensity is reached after about $3/\alpha$ of propagation distance within the medium, this band can be considered to be transparent with respect to the space-scale of interest (i.e. about 10^{-2} m). On the other hand, in the same temperature range the second band has low emissivity (accounting for the remaining 20%), but large absorption coefficient, hence it is able to reach in short distance the corresponding fraction of black-body intensity. When large absorption coefficients are present (again relative to the considered space-scale), the band is said to be diffusive. In practice, however, the two bands emit (or absorb) often similar values of intensity in the same distance, since the transparent one contributes a small fraction of a very large intensity value, while the diffusive one contributes a large fraction of a small intensity value.

The situation can change significantly for higher pressure values: in this case, the diffusive bands can have larger emissivity values at high temperature, meaning that they reach in short distance a significant portion of the black-body intensity (see Figure 11). This implies, roughly speaking, that at these pressure and temperature values a larger quantity of radiated heat is redistributed to the surroundings and transferred to the walls. Similar features as the one just presented apply for all the other mixtures that we considered.

Figure 12-(a) shows the dependency of the optimal partition of the EM spectrum, i.e. of parameter $\theta_{\hat{e}_{hf}}(\overline{p}, \overline{y}, \mu_1)$, on pressure. It can be noted that, as pressure increases, the boundary between the two bands shifts slightly and gradually towards lower frequencies, meaning that, for a given temperature, the second band accounts for larger fractions of the black-body intensity. This effect is clear also from the courses of the emissivities in Figures 10-11. In Fig. 12-(b), the optimal partitioning achieved with $M = 3$ bands is shown. It can be noted that the variation of the frequency cuts with pressure is less marked in this case, in particular for the boundary between the first and second bands. An example of the corresponding absorption coefficients and emissivities is shown in Fig. 13.

As regards the computational times required to compute a ROM, here are some figures obtained by running the order reduction algorithm on a workstation equipped with 12 Intel Xeon® cores at 2.4 GHz each and 52GB of RAM in total. The average time required to compute one set of coefficients for a given pressure and composition pair $(\overline{p}, \overline{y})$ was 0.23 hours for order-two models, and 0.32 hours for order-three models, in both cases with a temperature discretization with 50 nodes for the absorption coefficient, i.e. 101 and 152 optimization variables, respectively (see Section III-C2).

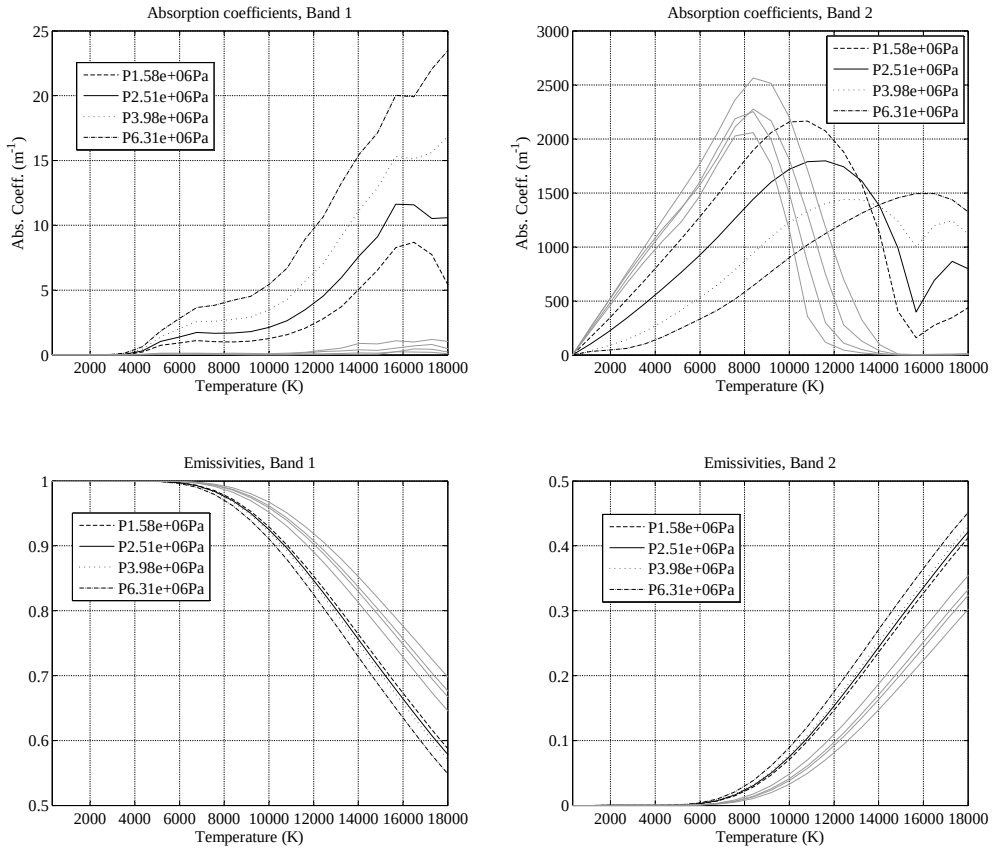

Fig. 11. Example of absorption coefficients and emissivities for a ROM with two bands for pure air. The gray lines correspond to the curves shown in Figure 10

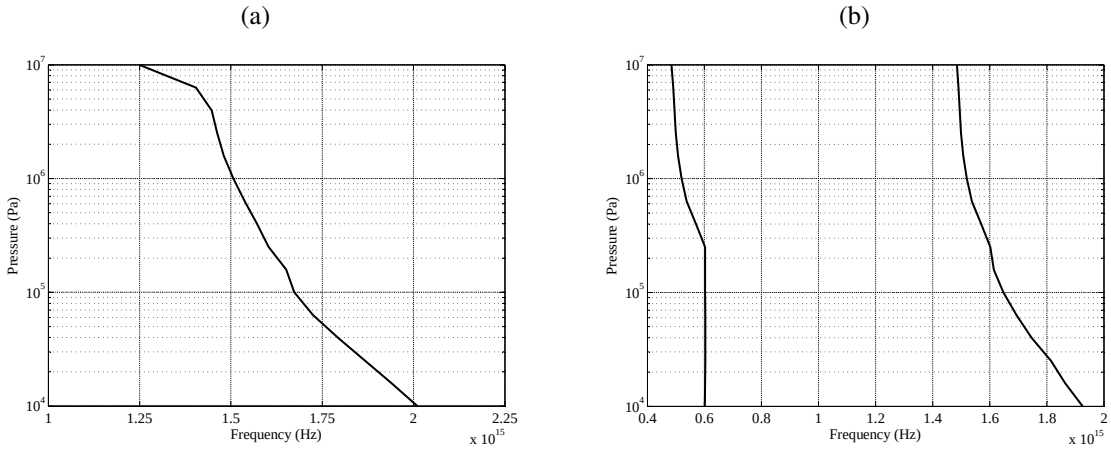

Fig. 12. Optimal partitioning of the frequency spectrum for pure air and (a) two bands, (b) three bands.

To give an idea of the accuracy achieved by the ROMs computed with the proposed method with respect to the FOM, we present two academic examples. The first one is related to the radiated heat intensity along a single line of propagation, with the temperature profile shown in Figure 14(a), through a mixture of 25% air, 50% copper and 25% hydrogen at $2.5\,10^5$ Pa. Such a profile is a realistic temperature distribution that can take place in the plasma generated during the switching process of a circuit breaker, and it was not part of the profiles $\tilde{T}_j$, $j = 1, \ldots, L_T$ used to derive the ROM coefficients. Two ROMs are considered, one with two bands and the other with three bands. The resulting distributions of the radiated heat intensity are shown in Figure 14(b). It can be noted that both ROMs are able to reproduce quite accurately the intensity profile given by the FOM, with the third-order one being slightly more accurate. This example thus shows that increasing the number of bands gives in general higher accuracy, but the gain is smaller and smaller

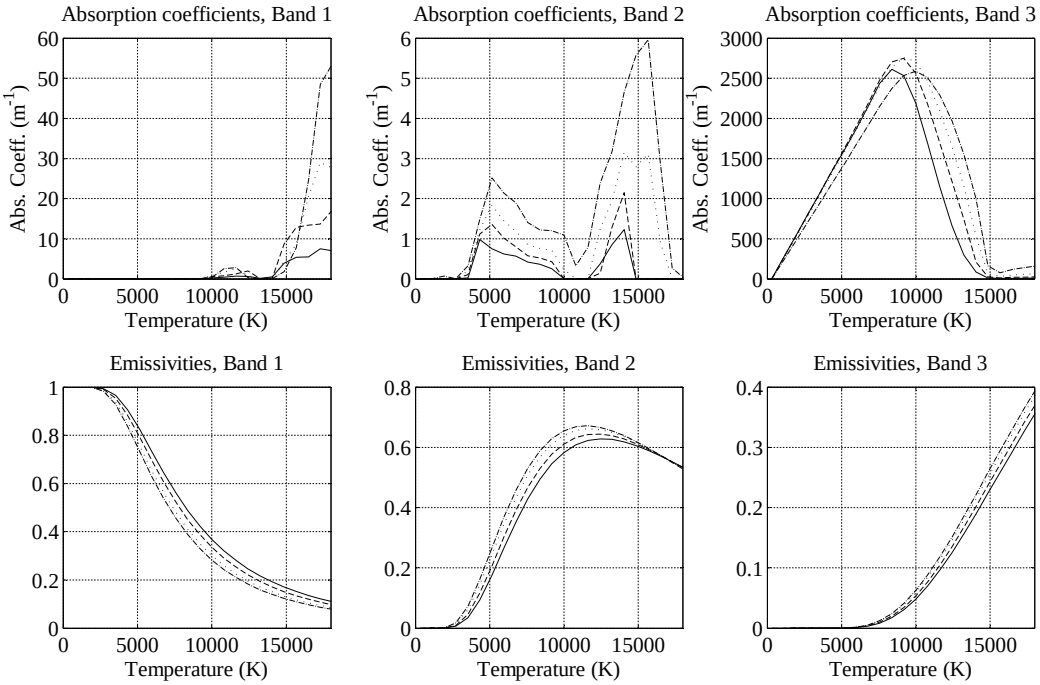

Fig. 13. Example of absorption coefficients and emissivities for a ROM with three bands for pure air. Pressure values: $2.51\,10^5$ Pa (solid lines), $3.98\,10^5$ Pa (dashed lines), $6.31\,10^5$ Pa (dotted lines), $1\,10^6$ Pa (dash-dotted lines).

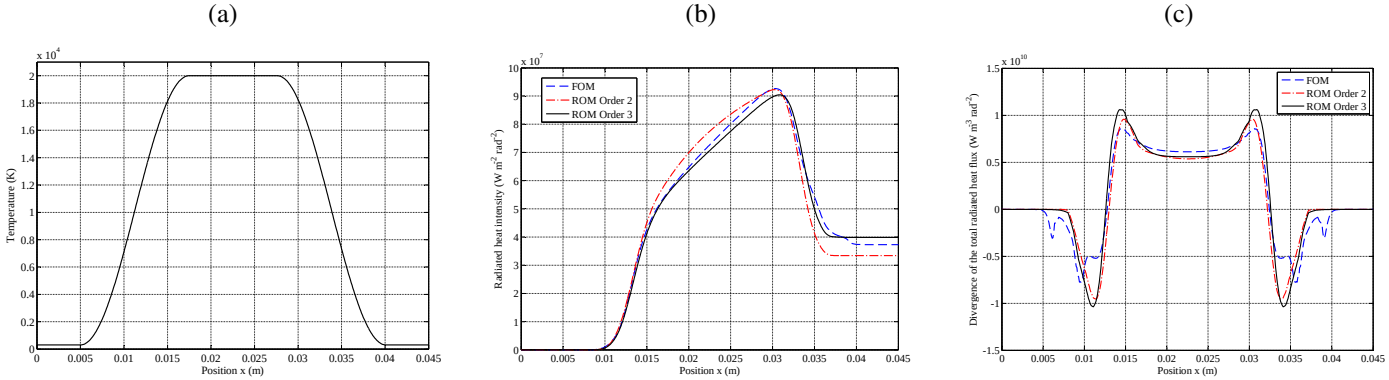

Fig. 14. (a) Temperature profile used to compare the radiated heat predicted by the FOM with that predicted by the ROM. (b) Comparison between the radiated heat intensities predicted by the FOM and the ones given by two ROMs with order 2 and order 3, respectively, using the temperature distribution of Figure (a). (c) Comparison between the divergence of the total radiated heat flux predicted by the FOM and by two ROMs, using the temperature distribution of Figure (a). Mixture: 25% air, 50% copper and 25% hydrogen at $2.5\,10^5$ Pa.

(in line with the considerations of Section II-B) and usually it is not worth using more than three bands, due to the increased computational load in the CFD simulations. Fig. 14(c) shows the divergence of the total radiated heat flux related to the 1D temperature profile of Fig. 14(a), i.e. considering the forward and backward propagation of the intensity. It can be noted that, although the divergence of the flux is not explicitly considered in the cost function used to compute the coefficients, the agreement is quite good for both the considered reduced-order models.

The second example is related to the use of the derived ROM for a discrete-ordinate method (DOM, see e.g. [35]) computation, where we want to compute the radiated heat intensity that reaches a wall in front of a column of hot gas composed by 75% copper and 25% air, at 10^5 Pa. Such a setup is described in Figure 15(a)-(b).

This example is more meaningful for the sake of CFD simulations of a plasma in real devices, where not just the intensity along a single line but the net total intensity obtained by integrating over all directions has to be computed, for each one of the finite volumes or elements that partition the computational domain. The intensity distribution (in W/m^2) on the wall is shown in Figure 16. It can be noted that the ROM is able to capture well the qualitative behavior given by the FOM, with an average error of about 10%. Such a value is indeed very small as compared with the accuracy that can be

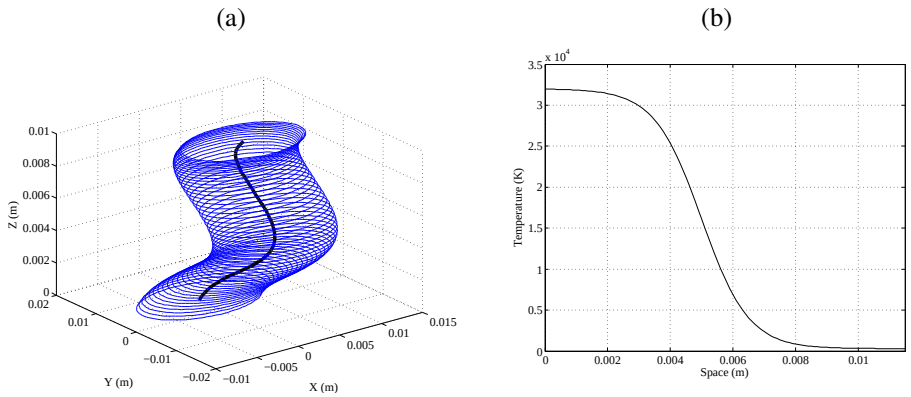

Fig. 15. Setup for a simulation of the radiated heat intensity using the discrete ordinate method. A column of hot gas (75% copper and 25% air at 10^5 Pa) is standing in front of a wall and we want to compute the radiated heat that reaches the wall. (a) Scheme of the setup, the wall of interest is parallel to the (Y, Z) and contains the point $(1.5\,10^{-2}, 0, 0)$. The column is represented by blue circles and the position of its center in (X, Y, Z) is shown as a solid black line. (b) Course of the temperature along a line parallel to the (X, Y) plane, passing through the center of the column, the highest temperature value corresponding to the column center.

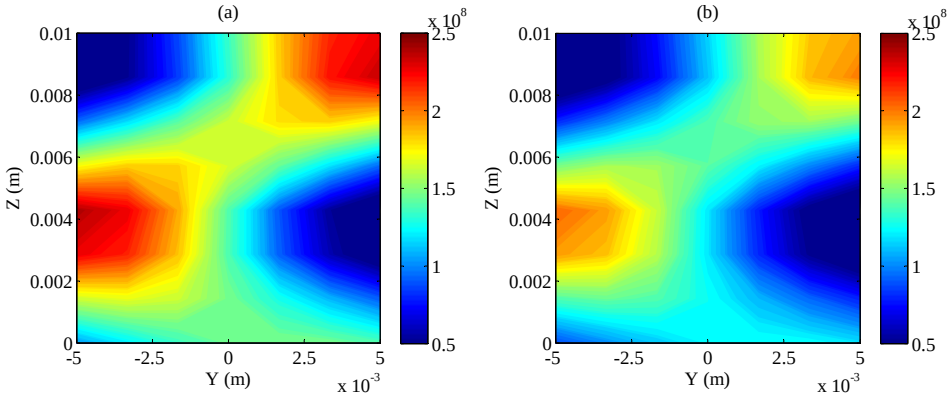

Fig. 16. Simulation results for the hot column example with the DOM method. Radiated heat intensity (W/m^2) that reaches the wall computed with the full-order model (left) and with a reduced-order model (right) with three bands and piecewise affine parametrization with 30 temperature nodes in the range $[300,\ 4\,10^4]$ K.

achieved with other approaches, e.g. using constant absorption coefficients over frequency bands.

Finally, in addition to the examples reported above, which are instrumental to showcase the typical output of our approximation procedure and the accuracy of the obtained reduced-order model with respect to the full-order one, we present next an example of results obtained by using the Arc Simulation Tool described in Section I-A to simulate a real-world industrial circuit breaker. Within the simulation tool, radiation affects the system's behavior mainly by means of two contributions: the divergence of the total radiated heat flux, which enters as a source (or sink) in the energy balance equation of the CFD solver, and the radiated heat exchanged between the plasma and the boundaries of the computational domain, which can be of different materials. Here, no results can be obtained with the FOM, due to the prohibitive computational time that would result if the finely resolved absorption spectrum were considered to calculate the radiation field. Thus, we show and briefly comment on the results obtained by using a two-bands ROM derived with the method described in this paper. The considered device is a circuit breaker with 1,600 A of nominal current, and the peak short-circuit current in the simulated test is about 20,000 A. We show the simulation results obtained with our tool at a given instant during the current interruption process, in particular at $7\,10^{-3}$ s after the initial opening of the contacts, when the conductive plasma is reaching the so-called splitter plates, i.e. metal plates meant to cool down the arc and dissipate its energy through surface erosion. Figure 17 reports the distributions of temperature, pressure, mass fractions of metal and of air in the plasma, showing that temperature and composition have a significant variability within the computational domain, while pressure differences are relatively moderate. The hot region where the electric arc is situated can be clearly recognized, with temperatures reaching 20,000K. The corresponding distribution of the absorption coefficients for the two bands of our ROM is shown in Figure 18: note that, as discussed above, one of the two bands tends to be transparent, with large absorption coefficients, and the other one diffusive in the hot region. Finally, the divergence of the radiative heat flux is depicted in Figure 19, divided into cooling and heating terms depending on its sign. In a way similar to the simple 1D example shown in Figure 14, one

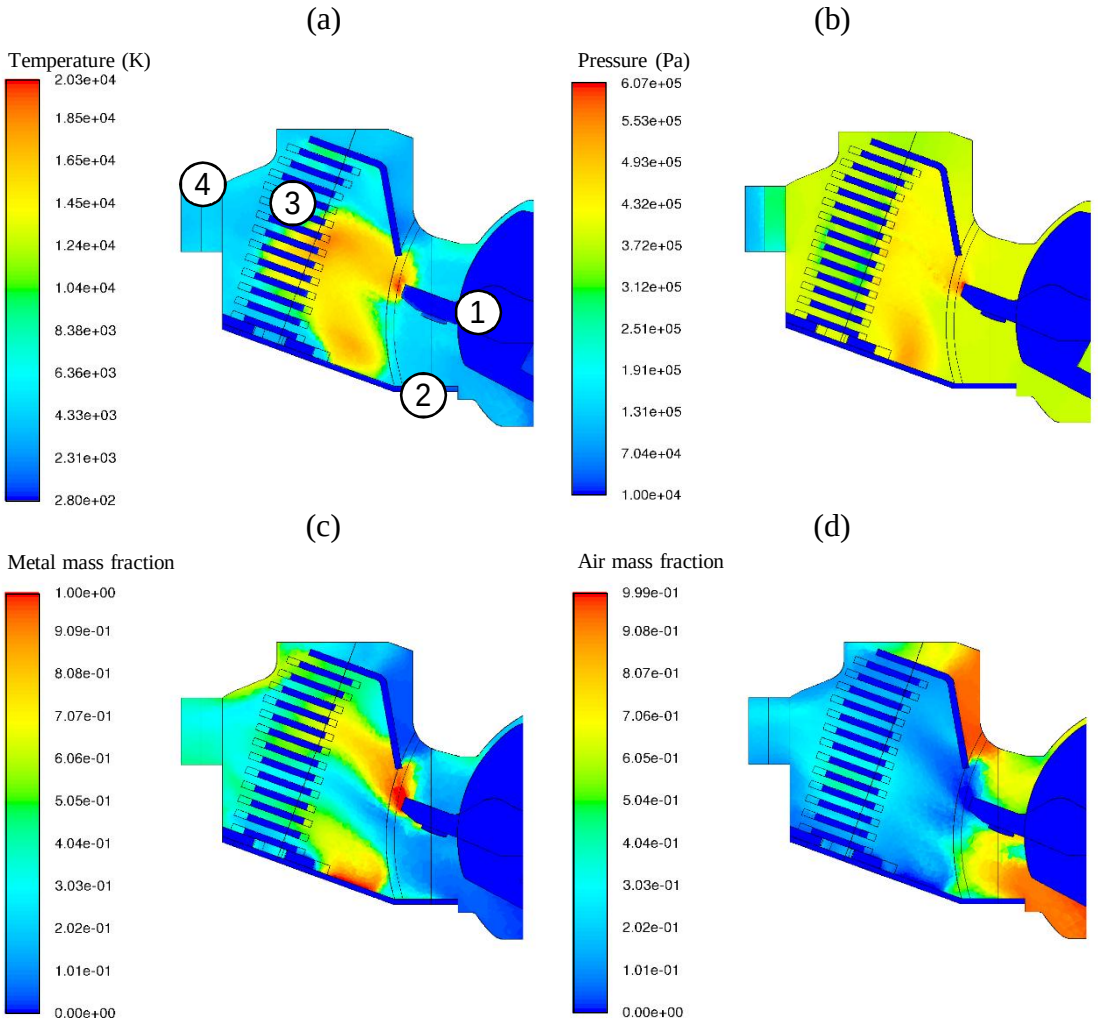

Fig. 17. CFD simulation results of a real-world circuit breaker during a short circuit. Distributions of (a) temperature, (b) pressure, (c) metal mass fraction in the plasma and (d) air mass fraction along the symmetry plane of the device. The moving contacts, fixed contact, splitter plates and device outlet are indicated in figure (a) with numbers 1, 2, 3 and 4, respectively. The mass fraction not accounted for by figures (c) and (d) is composed by hydrogen ablated from the polymeric components inside the breaker.

can clearly see from Figure 19 that the radiative heat tends to cool down the core of the arc and to heat its boundaries, while in the remaining part of the computational domain the contribution of radiation is negligible. In fact, the radiated heat which is not redistributed within the arc is transported to and absorbed by the solid surfaces that confine the arcing chamber.

V. Conclusions and Future Developments

We presented a new approach to derive reduced-order models of the radiative heat transfer through a participating gaseous medium. The approach is based on nonlinear identification and numerical optimization methods, and it can deliver models with low complexity but still accurate with respect to the original full absorption spectrum of the considered mixture. We also introduced a system-theoretic perspective of the phenomenon, as well as a frequency-domain analysis that justifies the use of low-order models to predict the total radiated intensity. We presented several comparisons between the full-order model and the reduced-order ones, as well as an example of results obtained with our 3D multi-physics tool for arc simulations in low voltage switchgear. With the proposed technique, one can reliably and systematically derive radiation models that can be used in CFD simulations of a plasma, since both the average absorption coefficients and the frequency bands are a result of the numerical optimization. The accuracy of the model depends mainly on the accuracy of the base data that the model approximates. A first subject of future research is thus the improvement and quality assessment of such base data.

Conceptually, our method is not different from other existing approaches to approximate radiative heat transfer, since all these techniques are based on some manipulation of the available, large-scale initial information to derive an approximation with manageable complexity, yet still accurate for the purpose of the specific application, see e.g. [38], [22]. An interesting question is then whether these approaches provide similar results, and if there are applications where one approach is more suitable than another. However, an in-depth comparison

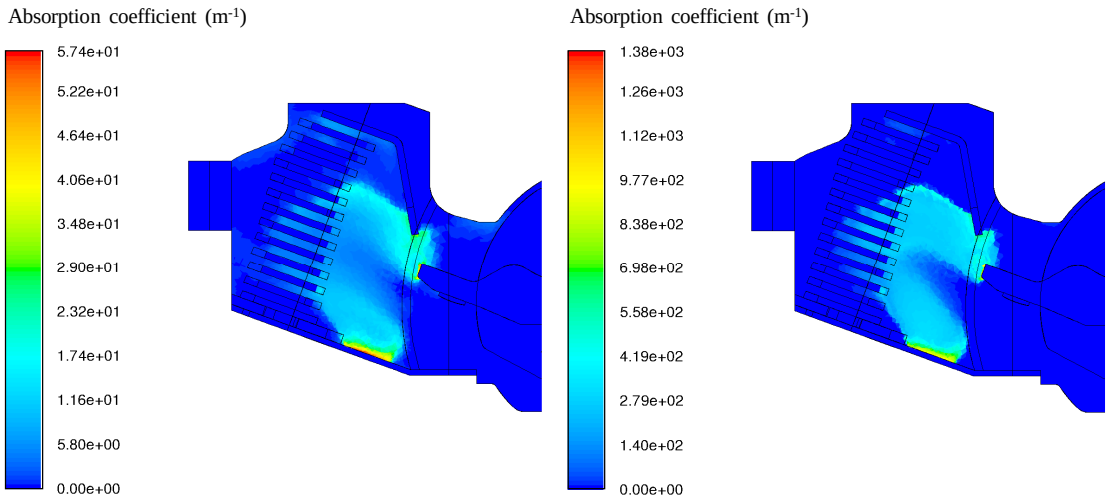

Fig. 18. CFD simulation results of a real-world circuit breaker during a short circuit. Distributions of the absorption coefficients for the first band (left) and for the second one (right).

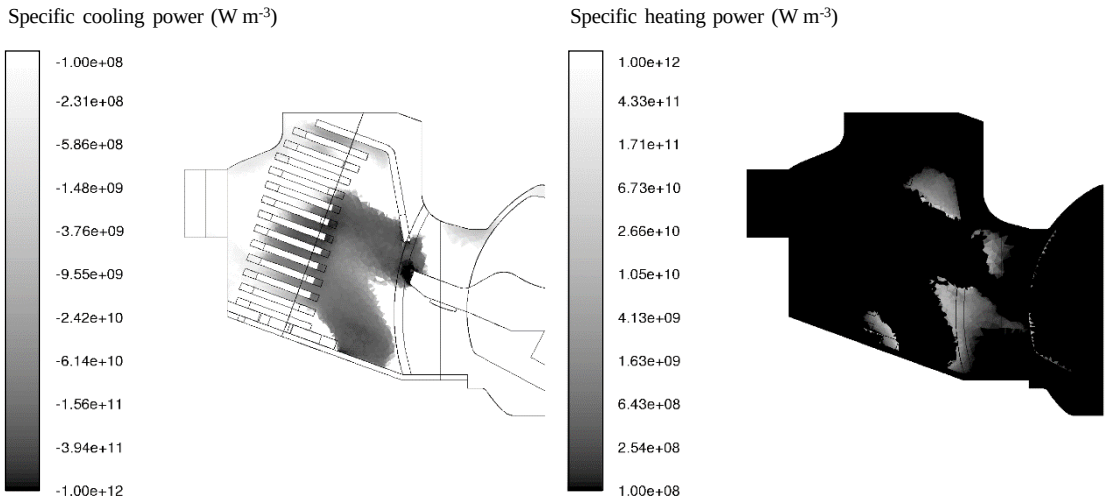

Fig. 19. CFD simulation results of a real-world circuit breaker during a short circuit. Cooling (left) and heating (right) terms due to the divergence of the total radiative heat flux.

would require a non-trivial effort to evaluate each technique on the same grounds, i.e. using the same base data for the absorption coefficients and tuning the involved parameters to achieve the best accuracy. Moreover, one should select test cases where the assumptions and settings considered by the various approaches hold. These assumptions are often driven by the application for which the approach is initially conceived. As an example, the approaches presented in [22] work best with narrow spectral ranges, they assume that in the considered range the absorption coefficients have a specific structure as a function of temperature, pressure and composition of the gas, they include scattering in the radiative transfer equation, finally they are applied to temperatures up to 3,000K. In our approach, so far we considered only broadband approximations, we don't have particular assumptions on the structure of the absorption spectrum and on its dependency on temperature, pressure and composition, we neglect scattering, and we are interested in temperatures up to 25,000-30,000K, which are typical in switching arcs when the circuit breaking device has to interrupt currents of the order of several thousand of A. While in principle the two techniques could be used for the same scope, a numerical comparison of their accuracy is clearly not trivial to obtain. Indeed, such comparisons represent a second interesting subject of future research.

ACKNOWLEDGEMENTS

The authors would like to thank Prof. V. Aubrecht for providing the absorption spectra used as base data in this study.

REFERENCES

[1] U. Al-Saggaf and G. Franklin. An error-bound for a discrete reduced-order model of a linear multivariable system. *Automatic Control, IEEE Transactions on*, 32:815–819, Aug 1987.

[2] M. Anheuser and C. Lüders. Numerical arc simulations for low voltage circuit breakers. In *XVIIIth Symposium on Physics of Switching Arc*, Nové Mesto na Morave, Czech Republic, 2009.

[3] V. Aubrecht and M. Bartlová. Radiation absorption coefficients in arc plasmas. *Czechoslovak Journal of Physics*, 54(3 supplement):C759–C765, 2004.

[4] V. Aubrecht and J.J. Lowke. Calculations of radiation transfer in SF6 plasmas using the method of partial characteristics. *Journal of Physics D: Applied Physics*, 27:2066, 1994.

[5] B. Bamieh and L. Giarré. Identification of linear parameter varying models. *International Journal of Robust and Nonlinear Control*, 12:841 – 853, 2002.

[6] N. P. Basse, M. Seeger, and T. Votteler. Quantitative analysis of gas circuit breaker physics through direct comparison of 3-D simulations to experiment. *IEEE Transactions on Plasma Science*, 36(5):2566–2571, 2014.

[7] M. S. Benilov. Understanding and modelling plasmaelectrode interaction in high-pressure arc discharges: a review. *Journal of Physics D: Applied Physics*, 41:144001, 2008.

[8] Bharat Heavy Electricals Limited. *Handbook of Switchgears*. McGraw-Hill, 2005.

[9] R. Bianchetti, A. Adami, L. Fagiano, R. Gati, and L. Hofstetter. Arc simulation in low voltage switching devices, a case study. *Plasma Physics and Technology*, 2(1):5–8, 2015

[10] T. Billoux, Y. Cressault, V.F. Boretskij, A.N. Veklich, and A. Gleizes. Net emission coefficient of CO2-Cu thermal plasmas: role of copper and molecules. *Journal of Physics: Conference Series*, 406:012027, 2012.

[11] S. Boyd and L. Vanderberghe. *Convex Optimization*. Cambridge University Press, New York, 2004.

[12] T. Christen and F. Kassubek. Minimum entropy production closure of the photo-hydrodynamic equations for radiative heat transfer. *Journal of Quantitative Spectroscopy and Radiative Transfer*, 110(8):452 – 463, 2009.

[13] M. Claessens and H.G. Thiel. CFD-simulation of high- and low current arcs in a self-blast circuit breaker. In *Physics of Power Interruption, IEE Colloquium on*, pages 8/1–8/3, Nové Mesto na Morave, Czech Republic, 1995.

[14] C. Doiron and K. Hencken. Calculation of thermodynamic and transport properties of thermal plasmas based on the Cantera software toolkit. In *The XXII Europhysics Conference on Atomic and Molecular Physics of Ionized Gases, ESCAMPIG XXII*, July 2014.

[15] W. A. Fiveland and A. S. Jamaluddin. Three-dimensional spectral radiative heat transfer solutions by the discrete-ordinates method. *Journal of Thermophysics and Heat Transfer*, 5:335–339, 1991.

[16] R. J. Goldston and P. H. Rutherford. *Introduction to Plasma Physics*. CRC Press, 1995.

[17] J. Heberlein, J. Mentel, and E. Pfender. The anode region of electric arcs: a survey. *Journal of Physics D: Applied Physics*, 43:023001, 2010.

[18] A. Iturregi, E. Torres, and I. Zamora. Analysis of the electric arc in low voltage circuit breakers. In *International Conference on Renewable Energies and Power Quality (ICREPQ '11)*, Las Palmas de Gran Canaria, Spain, 13-15 April 2011.

[19] C. Jan, Y. Cressault, A. Gleizes, and K. Bousoltane. Calculation of radiative properties of SF6-C2F4 thermal plasmas - application to radiative transfer in high-voltage circuit breakers modelling. *Journal of Physics D: Applied Physics*, 47:015204, 2014.

[20] L. Ljung. *System Identification - Theory For the User*. Prentice Hall, Upper Saddle River, N.J., 1999.

[21] J. Menart and S. Malik. Net emission coefficients for Argon-Iron thermal plasmas. *Journal of Physics D: Applied Physics*, 35:867, 2002.

[22] Michael F. Modest. Narrow-band and full-spectrum k-distributions for radiative heat transfer-correlated-k vs. scaling approximation. *Journal of Quantitative Spectroscopy & Radiative Transfer*, 76:69–83, 2003.

[23] B. Moore. Principal component analysis in linear systems: Controllability, observability, and model reduction. *Automatic Control, IEEE Transactions on*, 26:17–32, Feb 1981.

[24] O. Nelles. *Nonlinear System Identification: From Classical Approaches to Neural Networks and Fuzzy Models*. Springer Science & Business Media, 2001.

[25] J. Nocedal and S. Wright. *Numerical Optimization*. Springer, New York, 2006.

[26] H. Nordborg and A. A. Iordanidis. Self-consistent radiation based modelling of electric arcs: I. efficient radiation approximations. *Journal of Physics D: Applied Physics*, 41:135205, 2008.

[27] Nat. Inst. of Standards and Technology. NIST atomic spectra database, http://www.nist.gov/pml/data/asd.cfm, Last accessed 08/2014.

[28] J. Ostrowski, R. Bianchetti, I. Erceg-Baros, B. Galletti, R. Gati, D. Pusch, M. Schwinne, and B. Wüthrich. Computational magneto-hydrodynamics in the simulation of gas circuit breakers. *Int. J. of Computational Science and Engineering*, 9(5/6):433 – 444, 2014.

[29] J. Ostrowski, R. Hiptmair, F. Krämer, J. Smajic, and T. Steinmetz. *Transient Full Maxwell Computation of Slow Processes*, pages 87–95. Springer Science & Business Media, 2010.

[30] F. Reichert, J.J. Gonzalez, and P. Freton. Modelling and simulation of radiative energy transfer in high-voltage circuit breakers. *Journal of Physics D: Applied Physics*, 45:375201, 2012.

[31] P. K. Sahoo. *Magneto-hydrodynamics: Modeling and Analysis: Numerical and Computational Methods*. VDM Verlag, 2009.

[32] H. Sandberg and A. Rantzer. Balanced truncation of linear time-varying systems. *Automatic Control, IEEE Transactions on*, 49(2):217–229, Feb 2004.

[33] J.L. Schiff. *The Laplace Transform: Theory and Applications*. Springer Science & Business Media, 1999.

[34] J. Shercliff. *A Textbook of Magnetohydrodynamics*. Pergamon Press, 1965.

[35] R. Siegel and J.R. Howell. *Thermal radiation Heat Transfer, 3^{rd} Edition*. Taylor & Francis, Washington DC, 1992.

[36] R. Smeets, L. van der Sluis, M. Kapetanovic, D. F. Peelo, and A. Janssen. *Switching in Electrical Transmission and Distribution Systems*. Wiley, 2014.

[37] G. D. Wood, P.J. Goddard, and K. Glover. Approximation of linear parameter-varying systems. In *Decision and Control, 1996., Proceedings of the 35th IEEE Conference on*, volume 1, pages 406–411, Dec 1996.

[38] Hongmei Zhang and Michael F. Modest. A multi-scale full-spectrum correlated-k distribution for radiative heat transfer in inhomogeneous gas mixtures. *Journal of Quantitative Spectroscopy & Radiative Transfer*, 73:349–360, 2002.